

arXiv:2302.09576v1 [astro-ph.EP] 19 Feb 2023

Corresponding author: Kinsuk Acharyya
acharyya@prl.res.in

THE EFFECT OF METALLICITY ON THE NON-EQUILIBRIUM ABUNDANCE OF HYDROGEN DOMINATED EXOPLANET ATMOSPHERE

VIKAS SONI^{1,2} AND KINSUK ACHARYYA¹

¹*Planetary Sciences Division, Physical Research Laboratory, Ahmedabad, 380009, India*

²*Indian Institute of Technology, Gandhinagar, 382355, India*

Abstract

The atmospheric metallicity greatly influences the composition of exoplanet atmospheres. The effect of metallicity on the thermochemical equilibrium is well studied, though its effect on the disequilibrium abundance is loosely constrained. In this study, we have used the quenching approximation to study the effect of metallicity on the quenched abundance for a range of parameters (temperature: 500-2500 K, pressure: 10^{-4} - 10^3 bar, metallicity: 0.1 - $1000 \times$ solar metallicity). We determine the chemical timescale by finding rate limiting steps in a reduced chemical network with a network analysis tool and the thermochemical equilibrium abundance. The equilibrium abundance results are similar to the literature. The CO, H₂O, and CO₂ abundances increase with metallicity in the parameter range considered. The CH₄ abundance increases with metallicity for CO/CH₄ < 1 and is unaffected for CO/CH₄ > 1. The chemical timescale of CO shows minimal change with the metallicity, while the CH₄ chemical timescale is inversely proportional to atmospheric metallicity. The quench level of CO shifts into the high-pressure region, and the quench level of CH₄ shows complex behavior with metallicity. We benchmarked the quenching approximation with the 1D photochemistry-transport model for two test exoplanets (GJ 1214 b and HD 189733 b) and found it to be in good agreement. We also found that the quenching approximation is a powerful tool to constrain atmospheric parameters. We demonstrated this by constraining the metallicity and transport strength for the test exoplanets HR 8799 b, HD 189733 b, GJ 436 b, and WASP-39 b.

1. INTRODUCTION

Since the first discovery of exoplanets in 1992 (Wolszczan 1992), the database for exoplanets has been expanding rapidly. Characterizing the atmospheres of exoplanets ranging from Earth-like to gas-giants like Jupiter and finding atmospheric compositions and potential bio-signatures have become the fundamental facets of modern-day planetary sciences (Madhusudhan et al. 2016; Sing 2018; Fortney 2018; Helling 2019; Madhusudhan 2019). Molecules such as CO, CO₂, CH₄, H₂O, NH₃, HCN, which are the building blocks for more complex organic molecules and major reservoirs of elemental N, C, and O have already been detected in exoplanet atmospheres (Madhusudhan 2019). Observational spectra have been used in the retrieval models to constrain atmospheric abundances of these atmospheres (Madhusudhan and Seager 2009, 2011; Line et al. 2012; Kreidberg et al. 2014; Ranjan et al. 2014; Haynes et al. 2015; Benneke 2015; Stevenson et al. 2017; Rajpurohit et al. 2020). However, the abundances and detailed understanding of the formation of these molecules are most often model-dependent. The parameter space for reproducing the atmospheric composition of an exoplanet is degenerate due to uncertainty in factors such as the effects of interior processes, the T-P profile of the atmosphere, the efficiency of atmospheric dynamics, the presence of clouds and hazes, bulk metallicity, elemental ratios, among many others (Seager and Deming 2010; Madhusudhan et al. 2016).

The atmospheric elemental abundances, i.e., the presence of elements such as H, O, C, N, S, etc., vary significantly from one planet to another. If we look at the gas giants of the solar system, a large variation can be seen, and the general trend is that the atmospheric metallicity increases with decreasing mass. Metallicities for Jupiter, Saturn, Neptune, and Uranus are 3.3 - 5.5, 9.5 - 10.3, 71 - 100, and 67 - 111 \times solar metallicity, respectively, although large uncertainties exist in the abundances of individual elements (Atreya et al. 2018). For exoplanets, at the present sensitivity level, there is a large uncertainty, although several studies were made to discern metallicities from high-precision spectral analysis. Exoplanet metallicities vary from sub-solar (e.g., HAT-P-7 b, Mansfield et al. 2018), to comparable to solar (e.g, WASP-43 b, Stevenson et al. 2017), to moderately enriched (e.g., WASP-103 b, Kreidberg et al. 2018; WASP-127 b, Spake et al. 2021; WASP-121 b, Mikal-Evans et al. 2019; WASP-39 b, Ahrer et al. 2022) to significantly enriched (e.g., GJ 436 b, Knutson et al. 2014). Thus, even though only a small number of exoplanets are studied, the metallicity space appears to be diverse and can range between 0.1 to more than 1000 times solar metallicity (Wakeford and Dalba 2020).

The wide variation in atmospheric elemental abundances for exoplanets significantly affect the atmospheric compositions. However, due to the considerable variation in the various physical quantities such as pressure, temperature, transport strength, irradiation, and surface gravity, the signature of enriched/decreased metallicity vary significantly from one planet to the other. For example, the T-P profile of the planet decides the efficiency of a chemical reaction and the formation of chemical species. Besides various disequilibrium processes such as transport and photochemistry greatly alter the equilibrium compositions (Seager and Deming 2010; Madhusudhan et al. 2016). Studies have been undertaken to understand how varying elemental abundances affect the atmospheric properties and the equilibrium composition (Line et al. 2011; Madhusudhan and Seager 2011; Moses et al. 2011; Madhusudhan 2012; Moses et al. 2013a,b; Venot et al. 2014; Zahnle and Marley 2014; Charnay et al. 2015; Heng and Lyons 2016; Drummond et al. 2018). These studies are primarily divided into two classes; in one, the carbon to oxygen ratio (C/O) is varying (Moses et al. 2013a,b), and in the other,

the elemental abundances of O, C, N, etc., are increased/decreased compared to the solar values (Venot et al. 2014; Drummond et al. 2018; Charnay et al. 2015). Moses et al. (2013a) studied the effect of metallicity from 0.1 to $10^4\times$ solar metallicity for solar C/O ratio on the equilibrium abundance. The focus of their study is at a pressure of 100 mbar, since the infrared photospheres are present at this pressure. The study by Moses et al. (2013a) shows that the abundances of H₂O, CO, and CO₂ increase with metallicity, although the extent of this increase is different. In the CO dominant region, CO₂ increases as a square of the metallicity and becomes the dominant species at very high metallicity. In contrast, H₂O and CO increase linearly with metallicity. At very high metallicity, the H₂O abundance decreases as the overall availability of H decreases. Besides, CH₄ increases with metallicity at low temperature (where it is stable). Similar findings have been reported by Line et al. (2011); Zahnle and Marley (2014); Madhusudhan and Seager (2011); Moses et al. (2013b); Venot et al. (2014). In another study Charnay et al. (2015) found that for the H-rich atmospheres, the vertical mixing will increase as metallicity increases. Therefore, higher metallicity is required for a planet like GJ 1214 b to form condensate clouds in the upper atmosphere. Similarly, Drummond et al. (2018) used a coupled 3D hydrodynamic model to solve for the chemical equilibrium abundances and found that as the metallicity is increased, significant changes in the dynamical and thermal structure affect the phase curve. Also, the opacity effect is the dominant mechanism in altering the circulation and the thermal structure compared to the mean molecular weight and heat chemistry.

These general studies on the metallicity effect are limited to the equilibrium abundance or targeted for particular exoplanets where the disequilibrium processes are also considered. For example, the effect of metallicity on the disequilibrium abundance has been studied for the exoplanets GJ 436 b (Line et al. 2011; Madhusudhan and Seager 2011; Moses et al. 2013a; Venot et al. 2014); HD 18733 b and HD 209458 b (Moses et al. 2011; Dash et al. 2022); WASP-12 b, CoRoT-2 b, XO-1 b, and HD 189733 b (Moses et al. 2013b). However, the general behaviour of the metallicity on the nonequilibrium abundance is mostly unexplored.

In the presence of transport, the chemical species mix in different parts of the atmosphere. The abundance of species deviates from the equilibrium abundance if the timescale of the chemical reaction becomes larger than the timescale of the transport. The disequilibrium abundance due to transport is frozen at the equilibrium abundance at the quenched level. The quenching approximation is the most straightforward approach to estimate the disequilibrium abundance. In the quenching approximation, the quench level is defined at a pressure level where the chemical conversion timescale is equal to the vertical mixing timescale of the atmosphere. Below the quench level, the chemical timescale dominates over the transport timescale, and the atmospheric composition remains in the chemical equilibrium. Above the quench level, the abundance of the species is frozen with the equilibrium abundance at the quench level. However, one should apply the quenching approximation with caution, as the mixing length of the atmosphere cannot be calculated using the first principle approach. Also, the quenched molecules control the abundance of other molecules (Tsai et al. 2017; Moses et al. 2011; Smith 1998; Cooper and Showman 2006).

Thus the quenching approximation can be used as a powerful tool to understand the general behaviour of the effect of metallicities on non-equilibrium abundances. In this work, we aim to find the vertical mixing and the chemical timescales over the temperature range between 500 and 2500 K, the pressure range between 0.1 mbar and 1 kbar, and metallicity between 0.1 - 1000 .

× solar metallicity (-1 to 3 [Fe/H]). Then we use the timescale data to find the temperature and pressure space curve where these two timescales are equal (quenched curve) and study the quenched curve for various mixing strengths in the metallicity parameter space. In §2, the photochemistry-transport model is discussed, while in §3, the disequilibrium chemistry and the quenching approximation are discussed. The model results for both the equilibrium and disequilibrium chemistry are given in §4. A comparison between the quenching approximation results with the photochemistry-transport model is made in §5. Discussions are presented in §6 and the concluding remarks are made in §7.

2. 1D ATMOSPHERIC MODEL

We have developed a 1D photochemistry-transport model to study the atmospheric composition of exoplanets. In this section the main features of the model are briefly mentioned while a detailed description with benchmarking is provided in the Appendix. The model solves the mass continuity equation for each species as follows:

$$\frac{\partial n_i}{\partial t} = P_i - n_i L_i - \frac{\partial \phi_i}{\partial z}, \quad (1)$$

where n_i is the number density of the i -th species, P_i and $n_i L_i$ are the species production and loss rates due to chemical kinetics and photochemical reactions, and ϕ_i is the transport flux. The model couples the chemical kinetics and photochemistry with the atmospheric transport and solves equation 1 numerically for each layer and each species in the network till the convergence criteria take place. The transport processes include Eddy diffusion and molecular diffusion. The Eddy diffusion coefficient is taken as a parameter, and the molecular diffusion coefficient is calculated by the description given in [Chapman and Cowling \(1991\)](#). The upper atmosphere of exoplanets is exposed to stellar radiation, which produces free radicals that react with the other species and change the chemical composition. To find the flux in each atmospheric layer, we use the two-stream approximation of radiative transfer following [Heng et al. \(2014\)](#). In this method, we find the radiation flux, which is going out and coming in from both the boundaries of an atmospheric layer. This flux is converted into photon density and used to find the photochemical rates. We use the scattering and absorption cross-section data for active photochemical species in the network to find the optical depth.

The chemical network contains all the important species up to six hydrogen, two carbon, two nitrogen, and three oxygen atoms, and single atoms for He, Na, Mg, Si, Cl, Ar, K, Ti, and Fe. The chemical network is constructed by including chemical reactions involving H, C, N, and O from [Tsai et al. \(2017, 2018\)](#), while for the other elements, we have taken chemical reactions from [Rimmer and Helling \(2016\)](#). For this work we have used a reduced network of 52 species involving H-C-N-O which are connected by 600 chemical reactions.

To study the effect of metallicity on the nonequilibrium abundance of a hydrogen-dominated atmosphere, we make a grid in the metallicity, temperature, and pressure space. The pressure range is 10^{-4} to 10^3 bar, the temperature range is 500 to 2500 K, and the metallicity range is 0.1 to 1000 × solar metallicity. In this study, we change the metallicity relative to the solar photospheric elemental abundance. The change in metallicity corresponds to an increase or decrease in the heavy elemental abundance (elements other than H and He) with respect to the solar metallicity by a common factor. The solar photospheric metallicity is taken from [Lodders et al. \(2009\)](#). The range of bulk abundance of elements in the present study are $C/H = 2.77 \times 10^{-5} - 2.77 \times 10^{-1}$, $N/H = 8.18 \times 10^{-6} - 8.18 \times 10^{-2}$, and $O/H = 6.06 \times 10^{-5} - 6.06 \times 10^{-1}$.

We ran two sets of models. In the first set, we found the disequilibrium abundances in the presence of transport using quenching approximation, for which we followed the method given in Tsai et al. (2018). Then we used the method to discuss the effect of metallicity on the disequilibrium abundance and demonstrated how it can be used to constrain the metallicity and transport parameters, for which we used four test exoplanets, namely HR 8799 b, HD 189733 b, GJ 436 b, and WASP-39 b. In the second set, we ran the photochemistry-transport model for HD 189733 b and GJ 1214 b. We compared the output of the photochemistry-transport model with the quenching approximation which demonstrates the effectiveness of the quenching approximation.

3. DISEQUILIBRIUM ABUNDANCE AND QUENCHING APPROXIMATION

3.1. *Disequilibrium Abundance*

The presence of disequilibrium processes such as transport alter the atmospheric composition from its equilibrium abundance. In the transport-dominated region, the timescale for a chemical reaction becomes smaller than the timescale for atmospheric mixing; therefore, species transported from other layers cannot follow the equilibrium composition and the abundance deviates from equilibrium abundance, which has a large impact on the atmospheric composition. Prinn and Barshay (1977) used transport mixing to explain the high abundance of CO in the troposphere of Jupiter. Subsequently, a few different methods have been used to find the atmospheric composition in the presence of transport, and a comparison of these methods is given in Smith (1998). Among these methods, the quenching approximation is the most straightforward approach to constraining the disequilibrium abundance. It provides a way to determine disequilibrium abundance without running a full kinetics/transport model.

3.2. *Quenching Approximation*

The quench level is defined at a pressure level where the chemical conversion timescale is equal to the vertical mixing timescale of the atmosphere. Below the quench level, the chemical timescale dominates over the transport timescale, and the atmospheric composition remains in the chemical equilibrium. Above the quench level, the abundance of species is frozen with the equilibrium abundance at the quench level. The quenching approximation as described by Smith (1998) can give an accurate result within 15% of the kinetics/transport model (Moses et al. 2011). This approximation is routinely used in various studies to constrain the disequilibrium abundance of exoplanets (Madhusudhan and Seager 2011; Line et al. 2010; Moses et al. 2011; Visscher 2012; Zahnle and Marley 2014; Tsai et al. 2017, 2018; Fortney et al. 2020). We have used the quenching approximation to determine the abundance of CO, CH₄, H₂O, and CO₂ in order to study the effect of metallicity.

3.2.1. *Vertical Mixing Timescale*

The vertical mixing timescale τ_{mix} can be computed using the mixing length theory, and is given by the following equation:

$$\tau_{mix} = L^2/K_{zz}, \quad (2)$$

where L is the mixing length scale of the atmosphere and K_{zz} is the Eddy diffusion coefficient (Visscher and Moses 2011; Heng 2017). Since the Eddy diffusion coefficient has a large uncertainty, it is treated as a free parameter. The mixing length scale cannot be computed from the first principle,

and a simple approximation is to take the pressure scale height as the mixing length. However, [Smith \(1998\)](#) found that the mixing length can be $L \approx 0.1 - 1 \times$ pressure scale height, which leads to $\tau_{mix} = (\eta H)^2 / K_{zz}$, where $\eta \in [0.1, 1]$ and the exact value of η depends upon the rate of change of chemical timescale with height. The pressure scale height $H = \frac{K_b T}{\mu g}$, where T , g and μ are temperature, surface gravity, and mean molecular mass of the atmosphere, respectively. It is to be noted that metallicity changes the elemental composition, thereby changing the value of μ . When metallicity increases from 0.1 to $1000 \times$ solar metallicity, μ changes by one order of magnitude.

3.2.2. Chemical Timescale

In chemical equilibrium, the abundance of the chemical species does not change with time and the chemical reactions take place in a way that the production and loss rate of any species are balanced, such that

$$\frac{dn_{EQ}}{dt} = P_{EQ} - n_{EQ}L_{EQ} = 0. \quad (3)$$

Here, n_{EQ} , P_{EQ} and $n_{EQ}L_{EQ}$ are the number density, production and loss rate respectively and L_{EQ} is independent of n_{EQ} . When the physical conditions such as temperature and pressure of the system change, or the species are transported into other regions of the atmosphere, the chemical abundance deviates from chemical equilibrium, and the species are converted among themselves to restore chemical equilibrium. This conversion of species takes place through several chains of chemical reactions, which are called conversion schemes. The timescale of reactions in a conversion scheme can vary significantly; therefore, the conversion timescale is computed from the slowest reaction in the fastest conversion scheme, known as the rate-limiting step (RLS). The following relation gives the timescale of the conversion of species a into b :

$$\tau_{a \rightarrow b} = \frac{[a]}{\text{Rate of RLS}_{a \rightarrow b}}. \quad (4)$$

Here, $[a]$ is the abundance of species a , and $\text{RLS}_{a \rightarrow b}$ is the rate-limiting step in the conversion of a into b . In a chemical network, a particular species is involved in several reactions; as a result, there are many conversion pathways between two species. The number of these pathways increases exponentially as the number of reactions in the network increases. However, in a chemical network, only a few conversion schemes are important, as most of the conversion schemes are significantly slower than the fastest conversion scheme.

The timescale of the reactions is a function of several parameters, especially temperature and pressure. Therefore, as these parameters change, the RLS also changes, i.e., a reaction that is the RLS for a given set of parameters may not be the RLS as these parameters get altered. Thus the rate-limiting reaction can change in the parameter space. In order to understand the effect of metallicity on the RLS in the conversion between species, a chemical network analyzing tool is built. This tool takes a chemical network and finds all the possible conversion schemes between the species. It then finds the fastest conversion scheme and its slowest reaction (RLS). We adopted a reduced chemical network following [Tsai et al. \(2018\)](#) for this task and used their methodology. In [Figure 1](#), the conversion path between CH_4 and CO for the parameter range is shown. The different colored arrows (other than black) represent the RLS reactions. The RLS in the conversion of $\text{CH}_4 \rightleftharpoons \text{CO}$ for our parameter range of temperature, pressure and metallicity is listed below.

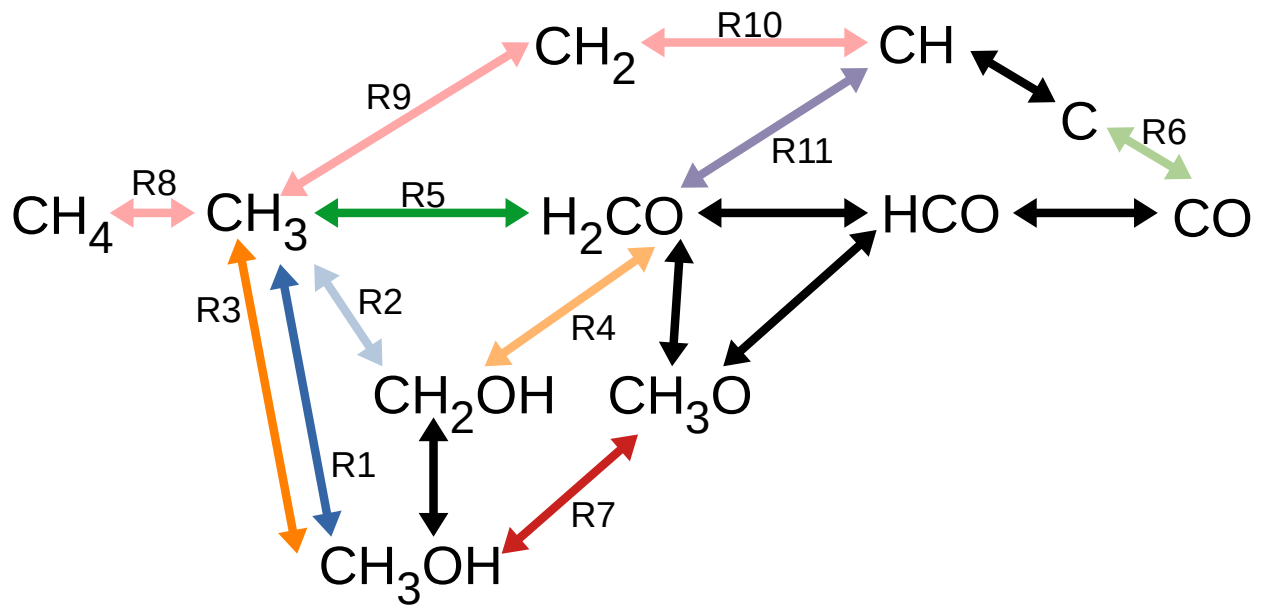
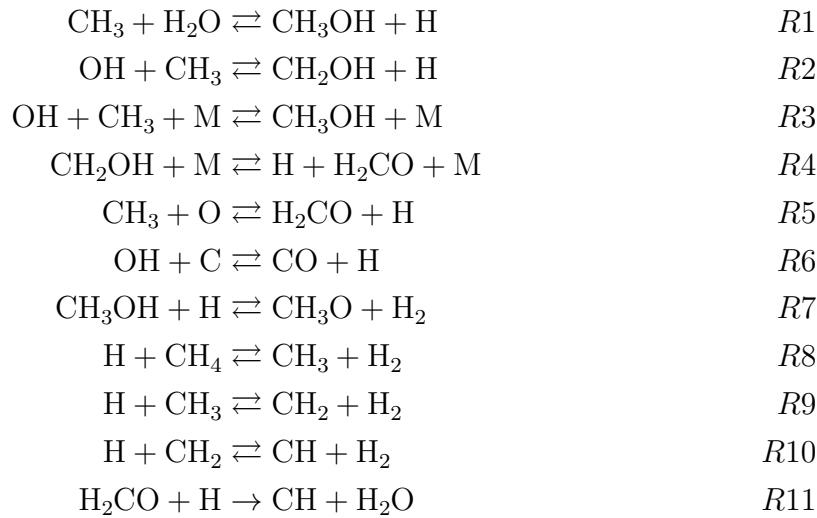


Figure 1. Major chemical pathways between CH_4 and CO for a hydrogen dominated atmosphere. The reactant is either H or H_2 from right to left, but the reactant is H_2O in the CH to H_2CO conversion. The colored arrows other than black are the rate limiting steps at different temperature-pressure values (see also Figure 5).

In the interconversion of $\text{CH}_4 \rightleftharpoons \text{CO}$, the chemical timescales are as follows (Tsai et al. 2018):

$$\tau_{\text{CH}_4} = \frac{[\text{CH}_4]}{\text{Reaction rate of RLS}} + \tau_{\text{H}_2} \times \frac{3[\text{CO}]}{\text{H}_2} \quad (5)$$

$$\tau_{\text{CO}} = \frac{[\text{CO}]}{\text{Reaction rate of RLS}} + \tau_{\text{H}_2} \times \frac{3[\text{CO}]}{\text{H}_2}. \quad (6)$$

Here, τ_{CH_4} and τ_{CO} are the timescales of conversion of $\text{CH}_4 \rightarrow \text{CO}$ and $\text{CO} \rightarrow \text{CH}_4$ respectively. $[\text{CH}_4]$, $[\text{CO}]$ and $[\text{H}_2]$ are the number densities of CH_4 , CO , and H_2 respectively. The interconversion timescale of $\text{H}_2 \rightleftharpoons \text{H}$ is τ_{H_2} , and ‘Reaction rate of RLS’ is the rate of RLS relevant for the desired temperature-pressure and metallicity values. The first term in equations 5 and 6 is related to the timescale of the RLS. The second term is related to the interconversion of $\text{H} \rightleftharpoons \text{H}_2$, which is necessitated because during the conversion of $\text{CH}_4 \rightleftharpoons \text{CO}$, the $\text{H} \rightleftharpoons \text{H}_2$ interconversion also occurs. Reconversion of $\text{H}_2 \rightarrow \text{H}$ or $\text{H} \rightarrow \text{H}_2$ is also required to achieve steady-state.

4. RESULTS

4.1. *Equilibrium Results*

We first re-visit the effect of metallicity on the chemical equilibrium abundances as described in Moses et al. (2013b). The chemical equilibrium abundance depends on the local temperature, pressure, and elemental abundance. It can be calculated by minimizing the Gibbs free energy of the system or by solving the mass continuity equation with the relevant chemical network for the parameter range. The chemical equilibrium composition can be used as the atmospheric composition when the chemical timescale is faster than the timescale of any other physical process; therefore, at the high-pressure and high-temperature region, the atmospheric composition can be approximated as the chemical equilibrium composition.

An increase in metallicity increases the bulk abundance of C and O, thereby increasing the abundance of molecules that use them. The effect of metallicity on the abundance can vary based on the use of heavy elements by molecules. For example, the metallicity dependence of molecules like CO, which consists of only one atom of each element, can be different from molecules like CO_2 , which requires two atoms of an element. Similarly, the metallicity dependence of molecules comprising one heavy element and hydrogen atoms, such as CH_4 and H_2O , will be different since the bulk abundance of hydrogen decreases at a slow rate with increasing metallicity; therefore, these molecules, can have a complex relationship with the metallicity. Although, the general behavior is that the abundance of the molecules with heavy elements increases with increasing metallicity, and the increase is more profound when the molecules consist of multiple heavy elements (Moses et al. 2013b). In Figure 2, the boundaries of $\text{CH}_4\text{--CO}$ and $\text{CO}_2\text{--CO}$ for 20 different metallicities are plotted. The boundary of $\text{CH}_4\text{--CO}$ shifts towards low temperature with metallicity, whereas the boundary of $\text{CO}_2\text{--CO}$ shifts towards high temperature. At 100 mbar pressure, the $\text{CH}_4\text{--CO}$ boundary shifts from 800 K to 600 K as the metallicity increases from 0.1 to $1000 \times$ solar metallicity. This behavior is similar as that obtained by Moses et al. (2013a).

In Figure 3, we have plotted the constant contour of the mixing ratio of CH_4 , CO , CO_2 , and H_2O in the metallicity and temperature parameter space at 100 mbar pressure. We have also over-plotted an equal-abundance curve of $\text{CH}_4\text{--CO}$, which divides Figure 3 into two regions. In region A, CH_4 dominates over CO (below the solid black line), while in region B, CO dominates over CH_4 (above the solid black line). The CH_4 abundance is increased in region A, whereas in region B, the CH_4 abundance is constant with metallicity. However, the decrease of bulk H at significantly high metallicity leads to a decrease in the CH_4 abundance. The CO abundance increases with metallicity for all temperature-pressure ranges. In region B, the CO abundance increases linearly with metallicity, and in region A, the increment rate increases as the temperature decreases. Available oxygen to form H_2O and CO is high in region A as compared to region B because in region B, atomic oxygen is

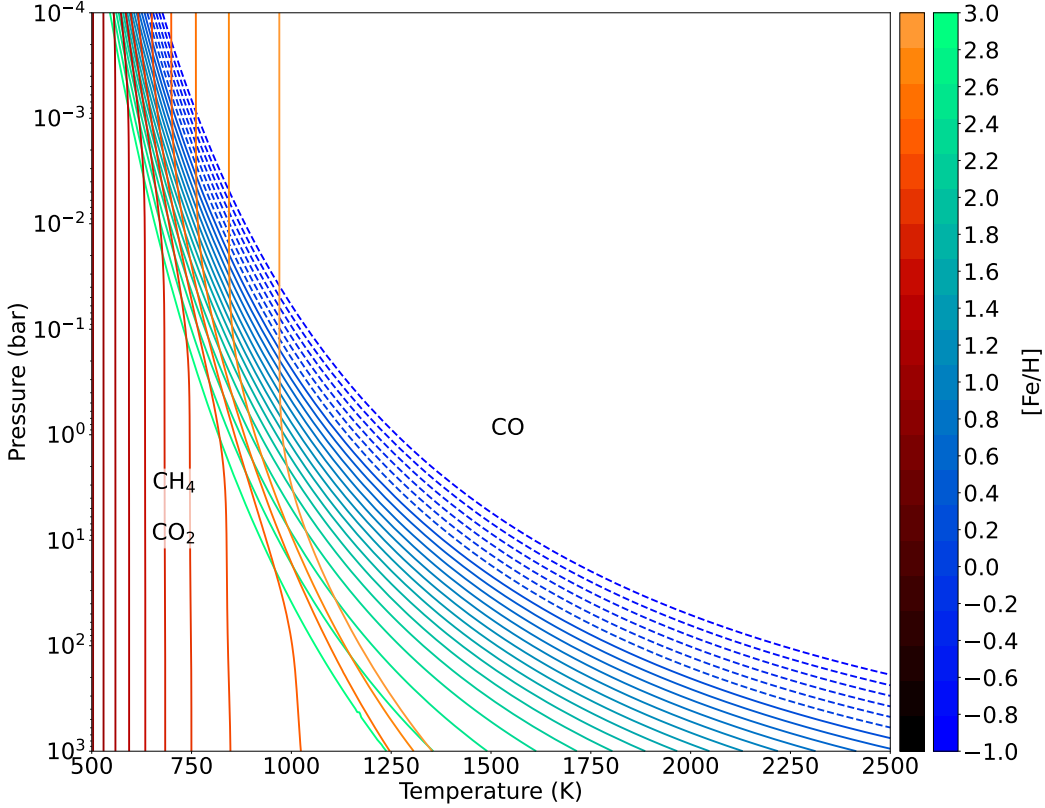


Figure 2. The contours of $\text{CH}_4/\text{CO} = 1$ and $\text{CO}_2/\text{CO} = 1$ for assorted metallicity values are shown. The cyan to blue lines delimitate the region where CH_4 (left) or CO (right) is the dominant species, and the orange to black lines delimitate the region where CO_2 (left) or CO (right) is the dominant species. The metallicity value in the colour bar corresponds to the respective colour line in the plot; for example, the rightmost curve for $\text{CH}_4/\text{CO} = 1$ represents $[\text{Fe}/\text{H}] = -1$, the second from right line corresponds to -0.8 , and so on. The dashed lines are for subsolar metallicity, and the solid lines are for supersolar metallicity. The subsolar metallicity lines for $\text{CO}_2/\text{CO} = 1$ are outside the parameter space.

locked in CO . For the solar C/O ratio, the O reservoir is almost twice that of the C reservoir; as a result, the H_2O abundance is linearly increased with metallicity (Moses et al. 2013a), since H_2O is among the most stable molecules in most of the temperature and pressure ranges. At $[\text{Fe}/\text{H}] > 3$, the increment of H_2O is restricted by the availability of the hydrogen reservoir. Also, in region B, the contours of the constant mole fraction of H_2O are at a relatively higher metallicity than in region A. The CO_2 abundance mostly follows the CO abundance in region A. However, in region B, the CO_2 abundance increases with the square of metallicity.

To understand the effect of metallicity on the pressure scale height of the atmosphere, contours of constant scale height in the temperature and pressure parameter space for 0.1 and $1000 \times$ solar metallicity and $g = 2000 \text{ cm s}^{-2}$ are shown in figure 4. It can be seen that the scale height has decreased only by one order of magnitude as the metallicity increases by four orders of magnitude. The change in the scale height is corresponds to the increase of the mean molecular mass of the atmosphere with increasing metallicity. The effect of metallicity on τ_{mix} comes from the dependence of mixing length on the pressure scale height (see section 3.2.1). τ_{mix} has a squared dependence on

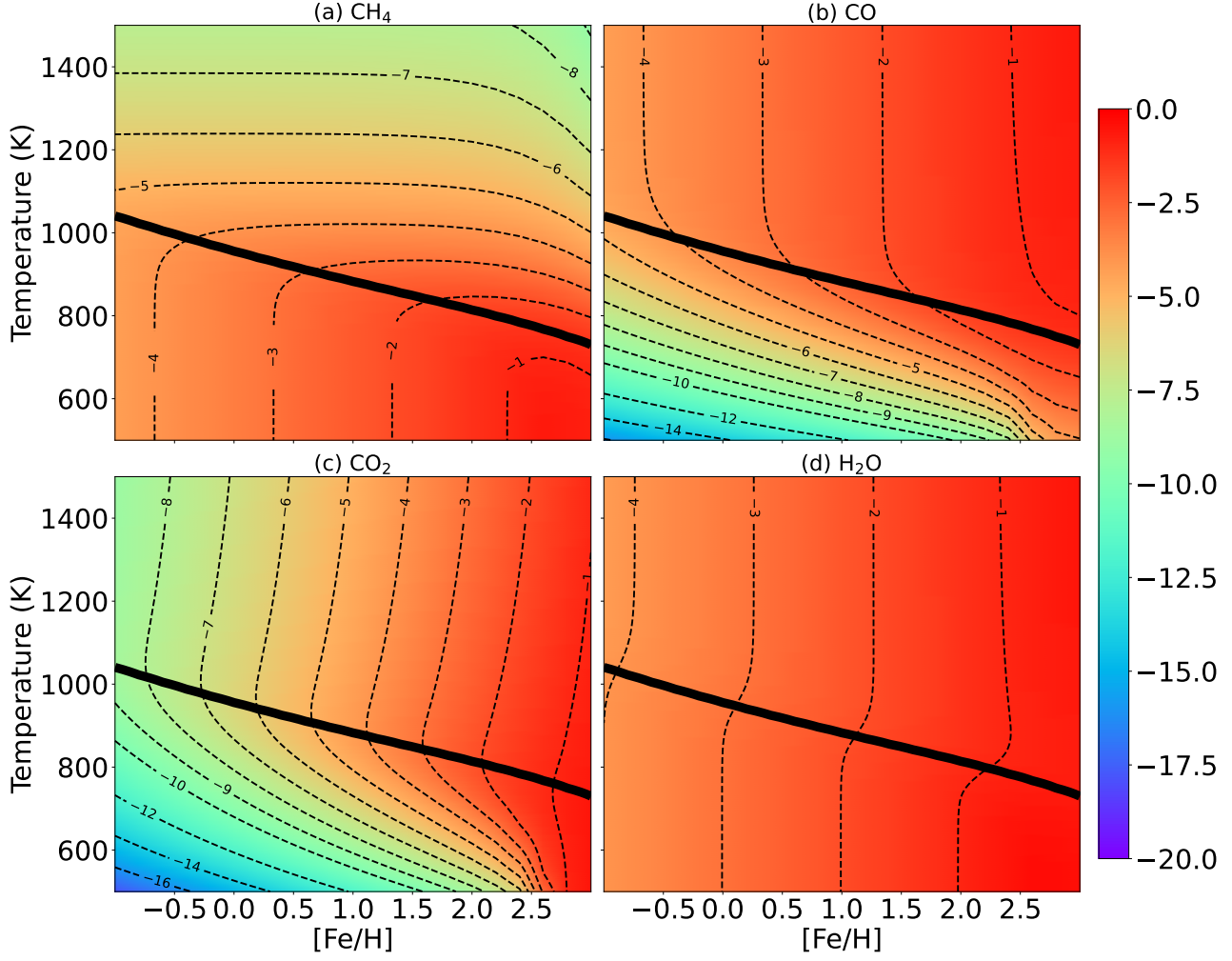


Figure 3. Variation of the equilibrium mole fraction for (a) CH_4 , (b) CO , (c) CO_2 , and (d) H_2O with metallicity and temperature at 100 mbar pressure is shown. The solid black line is the equal-abundance curve of CH_4 and CO , and the black dashed lines are the constant contours of the mole fraction (in log10 scale) of the respective gas-phase species.

the pressure scale height and the constant η can have a range of one order of magnitude; it makes τ_{mix} vary by four orders of magnitude as the metallicity increased from 0.1 to $1000 \times$ solar.

4.2. RLS and Disequilibrium Abundance

Figure 5 shows the effect of metallicity on the parameter space of the RLS reactions. Each coloured area represents the RLS reaction as shown in Figure 1. Maximum change occurs in the high-temperature and low-pressure region, where H is more stable than H_2 . In this region, CH_4 is converted into CO via progressive dehydrogenation and subsequent oxidation. The different steps of dehydrogenation become RLS as the metallicity increases. The pressure-temperature range for most of the RLS shift towards low temperature as the metallicity increases. It can be seen that R11 is only present in the $\text{CO} \rightarrow \text{CH}_4$ conversion but not in the $\text{CH}_4 \rightarrow \text{CO}$ conversion. Barring R11, all the RLS are common in both $\text{CO} \rightarrow \text{CH}_4$ and $\text{CH}_4 \rightarrow \text{CO}$ conversions. We find that the conversion

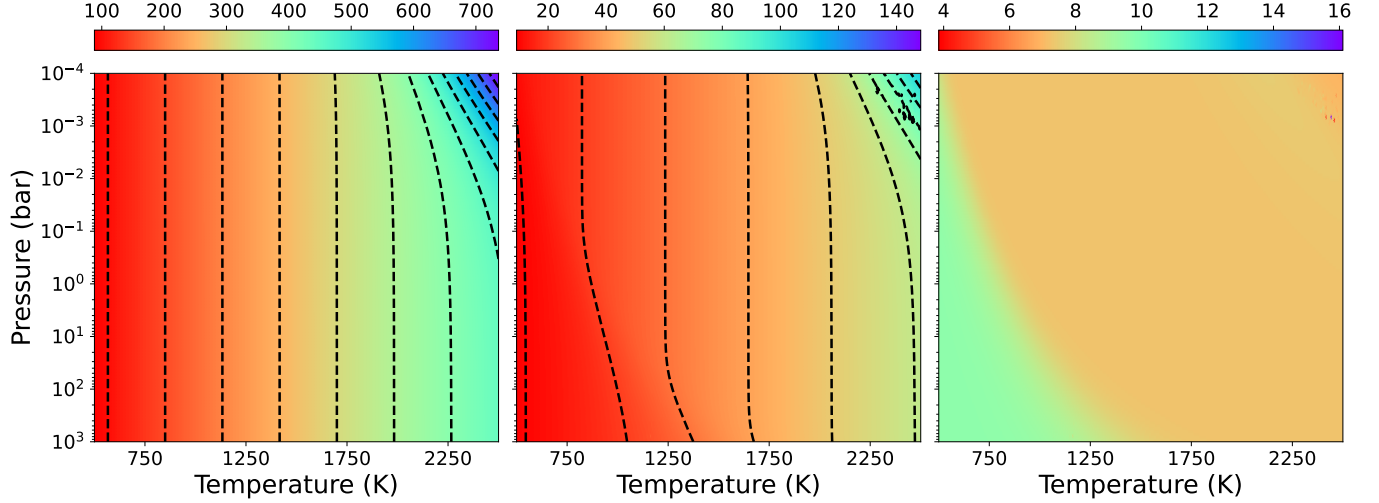


Figure 4. The constant contour lines for the scale height for two different metallicity values are plotted. The left panel is for $0.1 \times$ solar metallicity and the middle panel is for $1000 \times$ solar metallicity. The right panel is the ratio of 0.1 and $1000 \times$ solar metallicity.

pathways are the same as Tsai et al. (2018), though the RLS in the high metallicity region are slightly different.

Tsai et al. (2018) found three distinct pathways for the $\text{CH}_4 \rightarrow \text{CO}$ conversion. First, CH_4 is converted into CO through progressive dehydrogenation of CH_4 into C and further oxidization of C to form CO . Second, H_2CO forms by oxidation of CH_3 and converts into CO through HCO . Finally, third, the conversion path can differ depending on the temperature and pressure, and molecules like CH_2OH , CH_3OH , and CH_3O are intermediate molecules. We divided these RLS into two types based on the effect of metallicity on the RLS. In the first type, H or H_2 come as the reactants of the RLS. In the second, both the reactants of the RLS are heavy molecules. The abundance of H decreases with metallicity, but the relative change is slow. Thus the timescale of RLS in the first type increase slowly and the average abundance of heavy molecules increases linearly with metallicity (Zahnle and Marley 2014); in the second type, it is inversely proportional to metallicity.

4.3. Effect of Metallicity on the Conversion Timescale

4.3.1. CH_4 and CO Conversion Timescale

In Figures 6 and 7, we have shown τ_{CH_4} (Equation 5) and τ_{CO} (Equation 6) for four different temperatures (750 K, 1250 K, 1750 K, and 2250 K) and five different metallicities (0.1, 1, 10, 100, and 1000 $[\text{Fe}/\text{H}]$). The contributions from each term in Equations 5 and 6 i.e., the RLS (the first term in Equations 5 and 6) and the $\text{H} \rightleftharpoons \text{H}_2$ conversion term (the second term in Equations 5 and 6) are shown by the colored lines and the black dashed lines, respectively. The rates of increase of these two terms in Equations 5 and 6 are different, as is evident from Figures 6 and 7. In addition, their relative strengths are a strong function of temperature.

It can be seen that for the conversion of $\text{CH}_4 \rightarrow \text{CO}$, the relative importance of the $\text{H} \rightleftharpoons \text{H}_2$ conversion term changes profoundly over the parameter space. The magnitude of $\text{H} \rightleftharpoons \text{H}_2$ conversion term in equation 6 and 5 increases with increasing metallicity and decreases with increasing temperature and pressure. Although, the contribution for this term is lesser for the $\text{CO} \rightarrow \text{CH}_4$ conversion. It can

be seen that with an increase in metallicity and temperature, the point where the slope of $\text{H} \rightleftharpoons \text{H}_2$ conversion term changes in Figures 6 and 7 moves towards higher pressure region, indicating that it is moving from CH_4 to CO dominated region.

For 750 K (panel (a) in Figures 6 and 7), as the metallicity increases from 0.1 to $1000 \times$ solar, the contribution of the first term in Equation 5 is decreased by five orders of magnitude. In contrast, in Equation 6, the first term is increased by more than five orders of magnitude. The second term in Equation 5 dominates in the low-pressure region; for a given pressure, it increases with metallicity. The extent of increase is more in the high-pressure region when compared to the low-pressure region; in the high-pressure region, it increases by 15 orders of magnitude (Figure 7) when metallicity

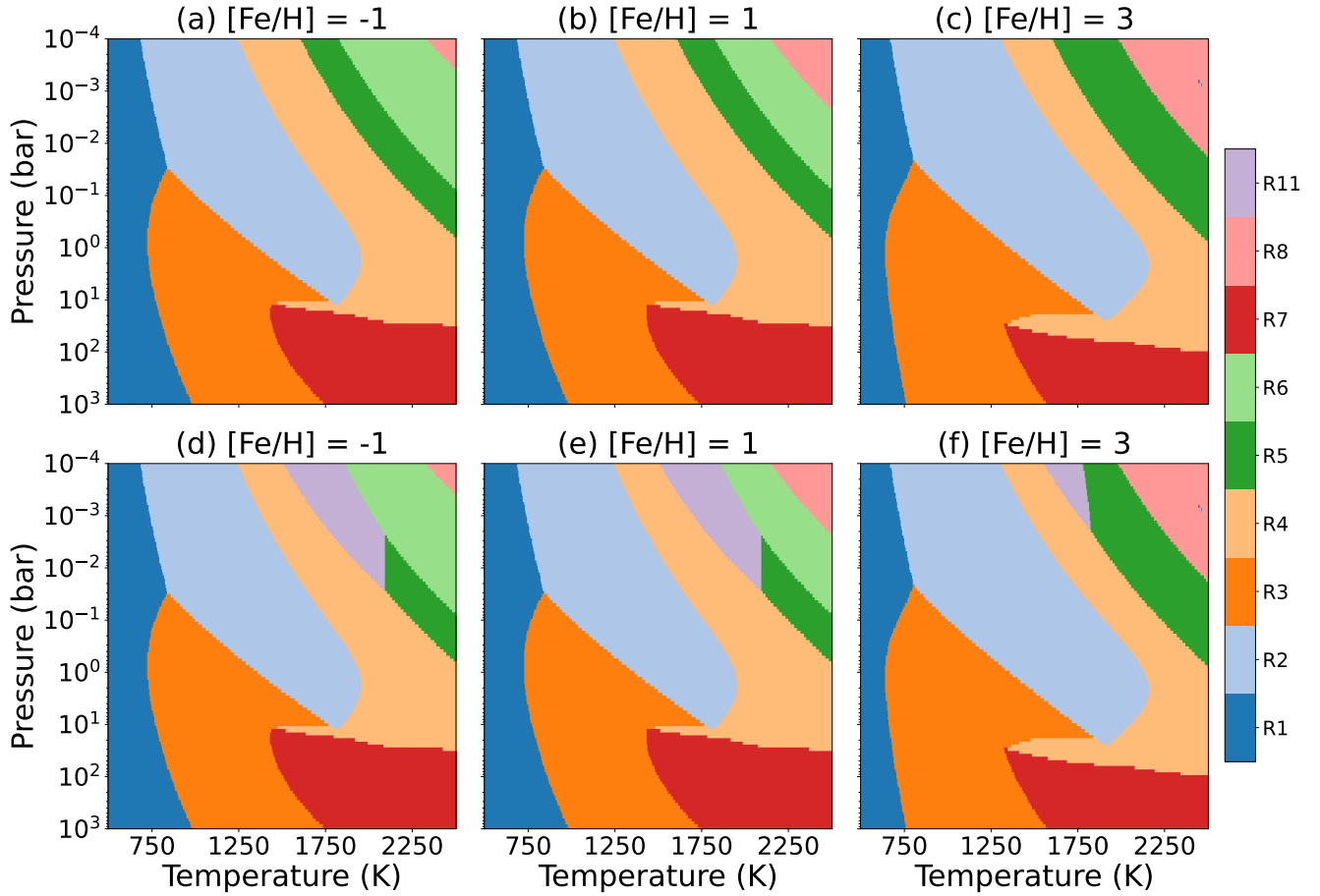


Figure 5. The temperature-pressure range of different rate-limiting steps is shown for three different metallicities. Each color corresponds to the different RLS in Figure 1. Panels (a)-(c) and (d)-(f) respectively represent the RLS parameter space for the conversion of $\text{CH}_4 \rightarrow \text{CO}$ (τ_{CH_4}) and $\text{CO} \rightarrow \text{CH}_4$ (τ_{CO}).

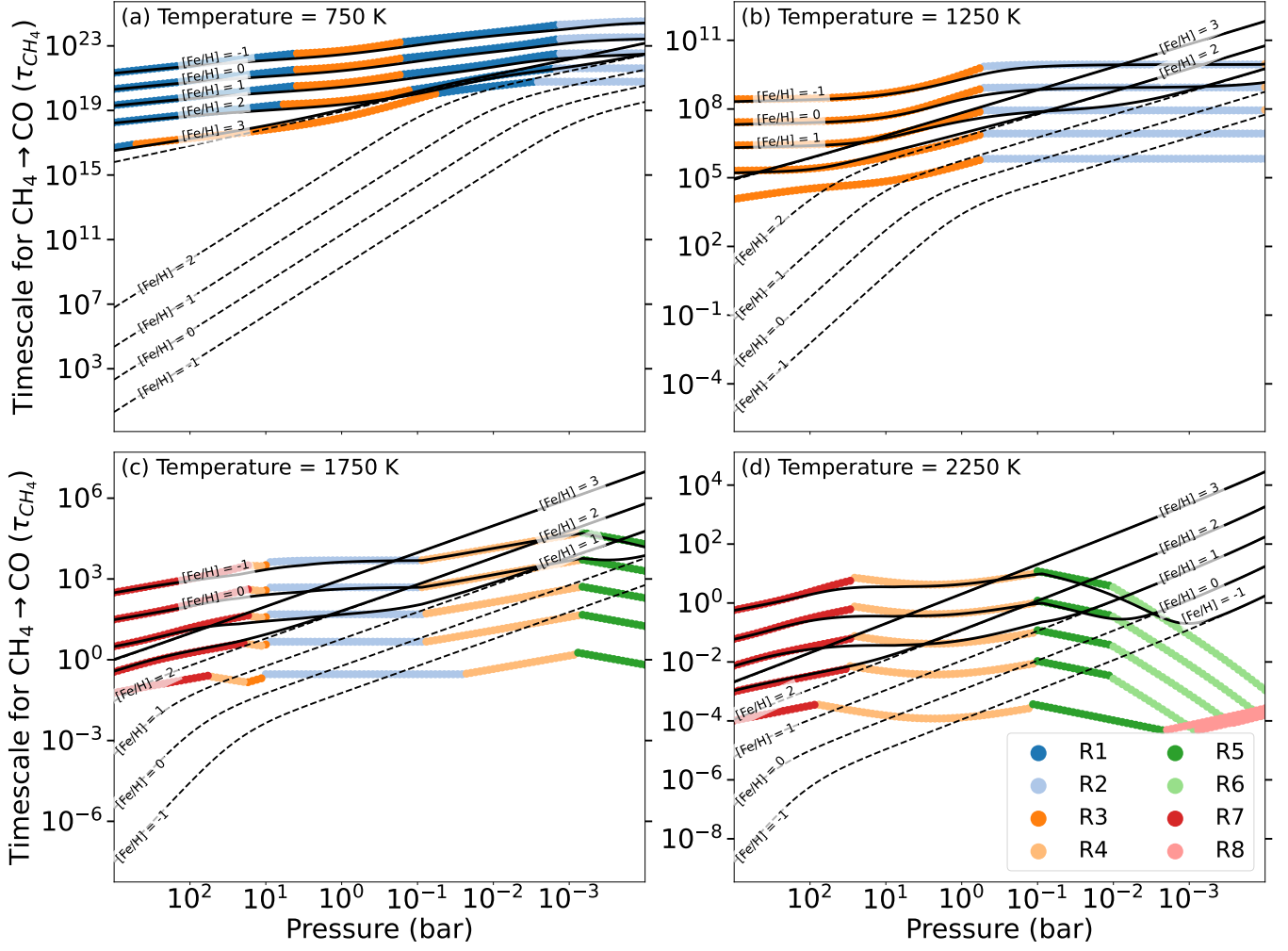


Figure 6. The timescale of conversion of $\text{CH}_4 \rightarrow \text{CO}$ (τ_{CH_4}) for four different temperatures (750 K, 1250 K, 1750 K, and 2250 K) with five different metallicities (0.1, 1, 10, 100, 1000 \times solar metallicity are shown). The colored lines represent the timescale of RLS in the corresponding temperature-pressure value, and the black dashed lines represent $\tau_{\text{H}_2} \times \frac{3[\text{CO}]}{\text{H}_2}$. The solid black line is τ_{CH_4} , labeled with the respective metallicity.

increases from 0.1 to 1000 \times solar value. Also, in this region, CH_4 dominates over CO ; with the gradual reduction in pressure, we move from the CH_4 to CO dominated region.

Panels (b), (c), and (d) in Figures 6 and 7 show the pressure variation of timescales for the temperatures 1250 K, 1750 K, and 2250 K, respectively. It is evident that as the temperature increases, the magnitude of these two terms starts to decrease. The metallicity dependence of τ_{CH_4} at a particular temperature remains qualitatively similar. The contribution of the first term in Equation 5 decreases by nearly five orders of magnitude with increasing metallicity for a given pressure. However, for τ_{CO} (Equation 6), the first term increases only slightly with an increase in metallicity (Figure 7) because for τ_{CO} the RLS belongs to the first type (see section 4.2). For τ_{CH_4} , with the increase of temperature, the contribution of the first term initially flattens out (1250 K) and then starts to decrease in the low-pressure region. Also, for τ_{CH_4} , the second term increases with metallicity by around 7 to 10 orders of magnitude for a given pressure, and it starts to dominate for a pressure of $\approx 10^{-3}$ bar

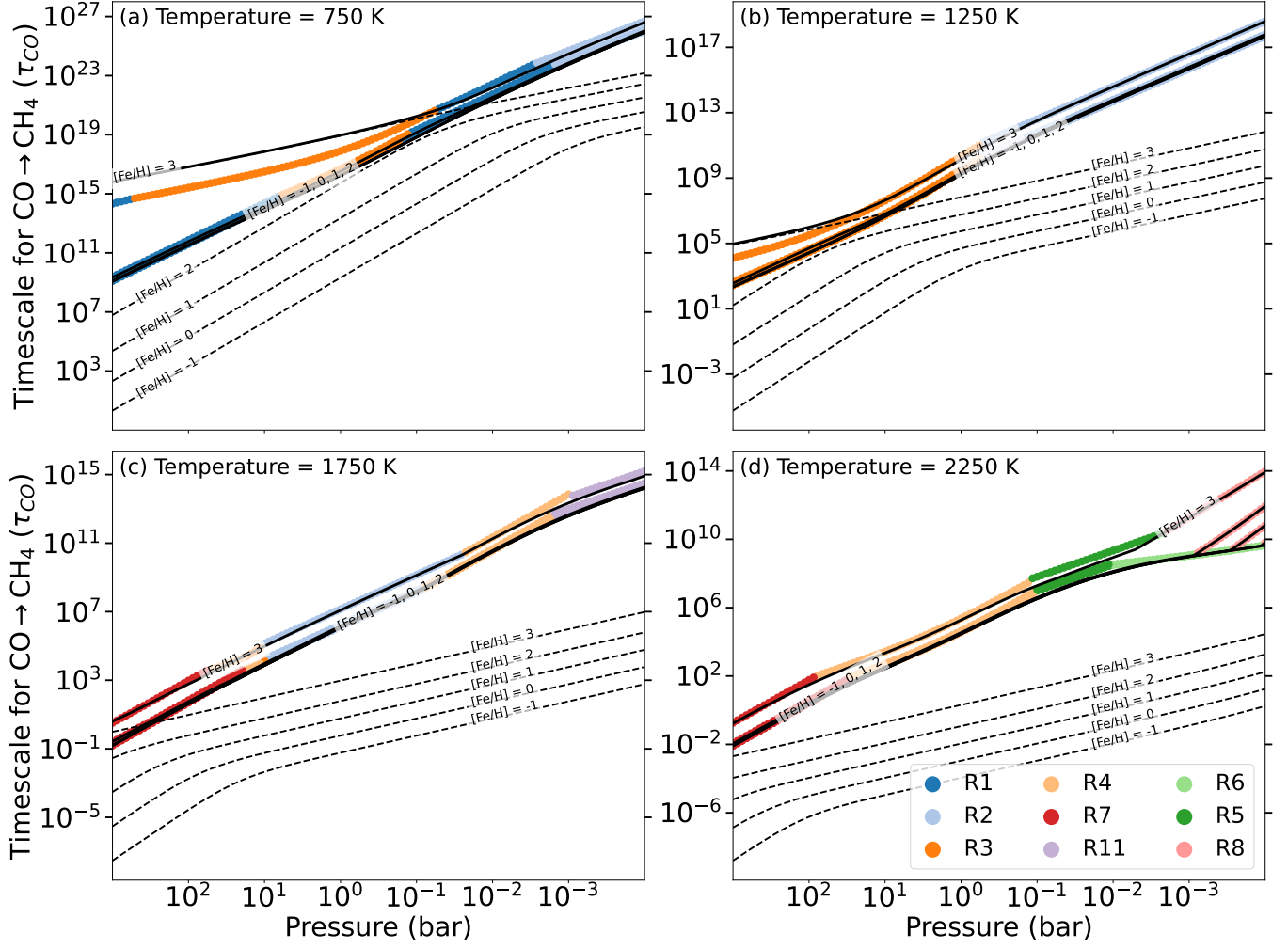


Figure 7. Same as Figure 6, but for CO \rightarrow CH₄ conversion.

but at different metallicities: $[Fe/H] > 2$, $[Fe/H] > 1$ and $[Fe/H] > -1$ for temperatures 1250 K, 1750 K and 2250 K, respectively. Thus, the $H_2 \rightleftharpoons H$ conversion term plays a more prominent role, especially in the low-pressure region for τ_{CH_4} , which makes the metallicity dependence complex. In comparison, the RLS term dominates most parts of the parameter space for τ_{CO} , thereby diminishing the contribution of the second term greatly.

In Figure 8, we have shown the constant contour lines of τ_{CH_4} and τ_{CO} in the temperature and pressure parameter space for four different metallicities. The solid, dashed, dotted, and dotted-dashed lines are for 1000, 10, 1, and $0.1 \times$ solar metallicity, respectively. The lines from blue to yellow are the constant contour lines of 10^0 to 10^{30} s. Both the conversion timescales decrease with increasing temperature and pressure. However, the dependence of the timescale on the metallicity is complex and has different dependencies at different pressure levels. The contours of constant τ_{CH_4} move towards the high-pressure region with an increment in metallicity in the region where the second term in Equation 5 dominates, since this term increases with metallicity. In the region where RLS is dominant, τ_{CH_4} is proportional to the metallicity and the contours of constant τ_{CH_4} move towards low temperature as the metallicity increases (see also Figures 6 and 7). In the region where R11 acts

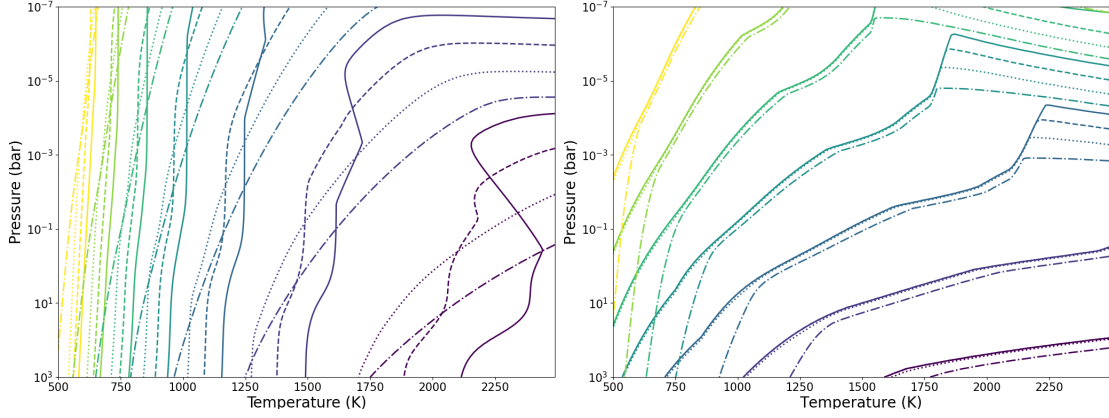


Figure 8. The constant contour line of τ_{CH_4} (left) and τ_{CO} (right) are plotted for four different metallicities (0.1, 1, 10, 1000 \times solar metallicity). The solid, dashed, dotted, and dotted-dashed lines show 0.1, 1, 10, and 1000 \times solar metallicity respectively. The coloured lines from blue to yellow represent the constant contour of timescales in log10 scale for 0, 5, 10, 15, 20, 25, and 30.

as the RLS, the contour of constant τ_{CO} shifts towards the high-pressure region with an increment in metallicity. For the intermediate pressure, temperature, and metallicity regions, τ_{CO} is unaffected by the metallicity. For $[\text{Fe}/\text{H}] < 2$, $T < 1250$ K and $P > 10^{-3}$ bar, the contour of constant τ_{CO} shifts towards the high-pressure region.

4.4. Effect of Metallicity on the Quench Level

To find the transport-induced disequilibrium abundances, we have used vertical mixing and chemical timescales and found the atmosphere's quench level (see section 3.2). At the quench level, the vertical

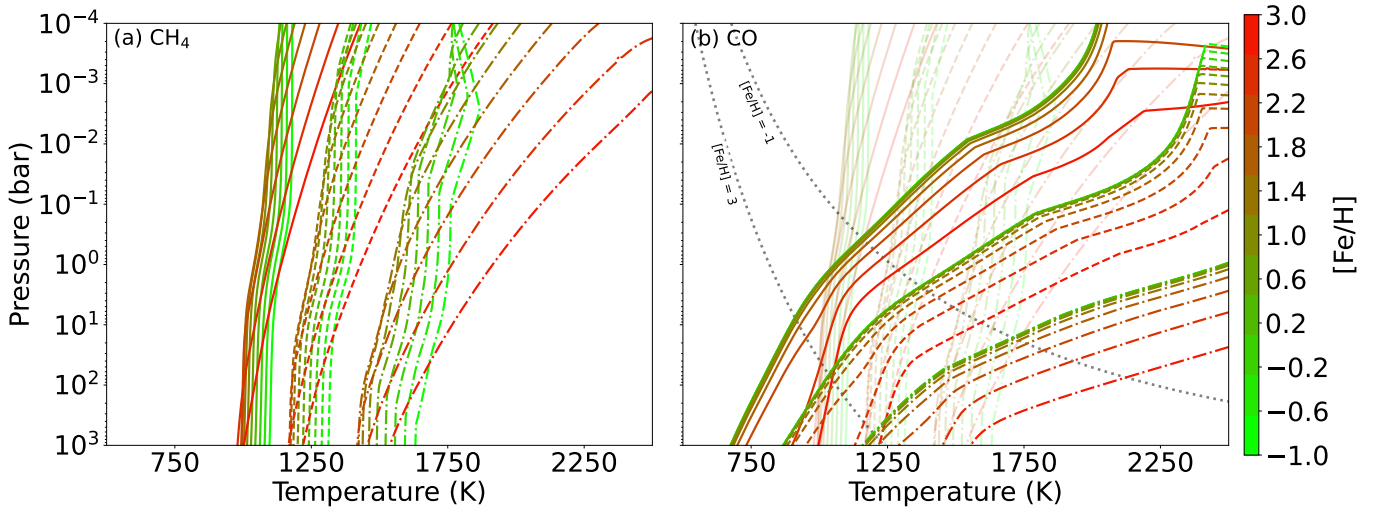


Figure 9. The contour of (a) $\tau_{\text{CH}_4}/\tau_{\text{mix}} = 1$ and (b) $\tau_{\text{CO}}/\tau_{\text{mix}} = 1$ for assorted parameters are shown. The colour bar (each value represents one metallicity contour) represents the metallicity value for the plotted quenched curve. The three sets of lines are for different values of K_{zz} coefficients; solid, dashed, and dashed-dotted lines are for $K_{zz} = 10^4$, 10^8 , and 10^{12} $\text{cm}^2 \text{s}^{-1}$ respectively. In panel (b), the quenched curves of CH_4 are shown in faded lines with the same colour and the equal-abundance curves for 0.1 ($[\text{Fe}/\text{H}] = -1$) and 1000 ($[\text{Fe}/\text{H}] = 3$) times solar metallicity are also shown.

mixing timescale is comparable to the chemical timescale. Since the chemical timescale is different for different species, the species quench at different atmospheric heights. Figures 9 (a) and (b) show the contour lines on which the vertical mixing and chemical conversion timescales are equal for CH₄ and CO, respectively. The three sets of lines are for different values of K_{zz} coefficients (solid: 10^4 cm² s⁻¹, dotted: 10^8 cm² s⁻¹, and dashed-dotted: 10^{12} cm² s⁻¹). Each set of lines runs from green to red (shown in the color bar), representing eleven different metallicity values. The figure shows both species' general behavior of vertical mixing and chemical timescales. As the temperature and pressure increase, the chemical timescale decreases; therefore, for quenching to happen, the corresponding vertical mixing timescale also has to reduce, which will require a higher K_{zz} value. It is evident from Figure 9 that as we move towards the high pressure and temperature regions, K_{zz} increases. For each K_{zz} value, the quenched curve for eleven different metallicities are shown. The vertical mixing timescale decreases with increasing metallicity, leading to shifting of the quenched curve in the high temperature and high-pressure region with increasing metallicity. However, the effect of metallicity on the chemical timescale is complex, making the quenched curve a complex function of metallicity. For a fixed K_{zz} value, the CO quenched curve shifts towards the lower atmosphere with increasing metallicity and follows τ_{CO} for 10^3 - 10^{-4} bar and 500 - 2500 K. Increasing the metallicity decreases the vertical mixing timescale, but τ_{CO} mostly remains constant. As a result, the quenched curve of CO moves from the low-pressure to the high-pressure region in the parameter space. In the CH₄ → CO conversion, τ_{CH_4} shows complex behavior with metallicity, which is also reflected in Figure 9 (a). The quenched curve shifts towards the low-temperature and low-pressure region for the parameter region in which the first term dominates in Equation 5. However, when the second term dominates, the quenched curve moves to the higher-pressure region with increasing metallicity.

4.4.1. H₂O

For solar C/O ratio, atomic oxygen is more than twice as abundant as C (Lodders et al. 2009). Therefore even if all the C is locked into CO, the available atomic oxygen to form H₂O does not decrease significantly. Thus, water is the most abundant O-bearing species for the parameter space, as pointed out by Moses et al. (2013a). Quenching will not affect the H₂O abundance, as it remains dominant at the quench level (Moses et al. 2011) and follows its chemical equilibrium abundance. In Figure 10, we have shown the different regions of the RLS and the pathways for the H₂O → CO conversion. The conversion of H₂O → CO has mainly two pathways. In the first pathway, the atomic carbon to form CO comes from CH₄, and the RLS in this conversion is the same as in the CH₄ → CO conversion and reactions R1 to R5 become the RLS. In the second pathway, C comes from CN or HCN to form CO. The increment of metallicity significantly increases the second pathway. This is because increasing the metallicity decreases the relative abundance of CH₄, resulting in the relatively lower reaction rate of RLS in the conversion of CH₄ → CO. The timescale of H₂O or $\tau_{\text{H}_2\text{O}}$ is given as follows:

$$\tau_{\text{H}_2\text{O}} = \frac{[\text{H}_2\text{O}]}{\text{Reaction rate of RLS}} + \left(\tau_{\text{H}_2} \times \frac{3[\text{CO}]}{\text{H}_2} \text{ or } \tau_{\text{NH}_3} \times \frac{[\text{CO}]}{\text{NH}_3} \right), \quad (7)$$

where the $\tau_{\text{H}_2\text{O}}$ is the timescale of conversion of H₂O → CO, and [H₂O], [CO], [NH₃] and [H₂] are the number densities of H₂O, CO, NH₃ and H₂ respectively. τ_{H_2} is the interconversion timescale of H₂ ⇌ H and τ_{NH_3} is the timescale of NH₃ + H → NH₂ + H₂. The second term is either $\tau_{\text{H}_2} \times \frac{3[\text{CO}]}{\text{H}_2}$ or

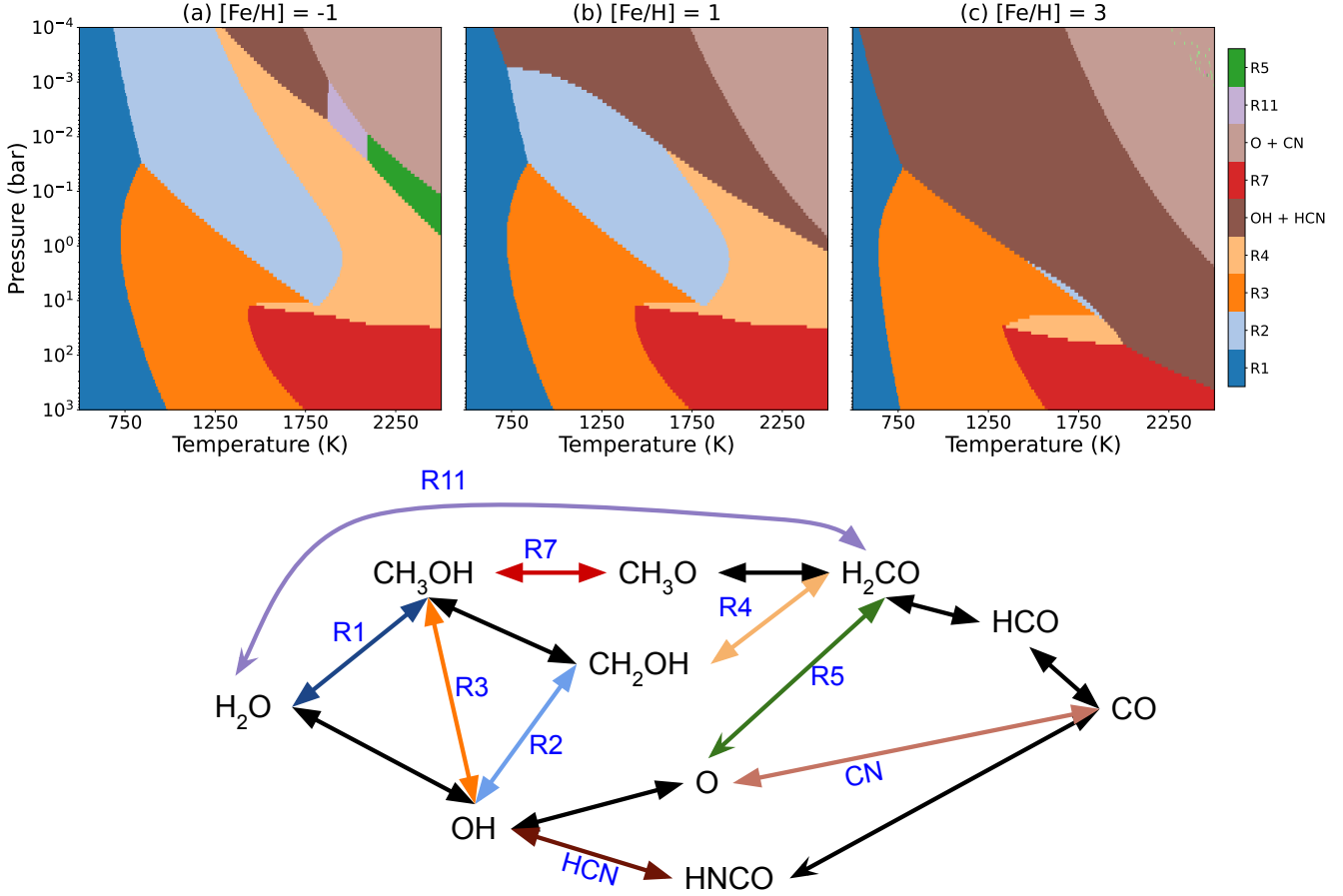


Figure 10. The top row shows the temperature-pressure range of different rate-limiting steps for the conversion of $\text{H}_2\text{O} \rightleftharpoons \text{CO}$ for three different metallicities. The colored regions correspond to the RLS in the bottom plot which shows the major chemical pathways for $\text{H}_2\text{O} \rightleftharpoons \text{CO}$ conversion in hydrogen dominated atmosphere.

$\tau_{\text{NH}_3} \times \frac{[\text{CO}]}{[\text{NH}_3]}$, which is decided by the temperature-pressure range. When atomic carbon for CO comes from CH_4 , then $\tau_{\text{H}_2} \times \frac{3[\text{CO}]}{[\text{H}_2]}$ is used whereas, if it comes from HCN or CN, then $\tau_{\text{NH}_3} \times \frac{[\text{CO}]}{[\text{NH}_3]}$ is used.

In Figure 11, we have shown $\tau_{\text{H}_2\text{O}}$ (Equation 7) for four different temperatures (750 K, 1250 K, 1750 K, and 2250 K) and five different metallicities (0.1, 1, 10, 100, and 1000 \times solar). The RLS term, i.e., the first term in Equation 7 dominates over the second term for all the temperature and pressure regions. $\tau_{\text{H}_2\text{O}}$ is slower than τ_{CO} and τ_{CH_4} for all the temperature-pressure ranges, which makes the quench level of H_2O lie deep in the atmosphere. However, it is to be noted that if C/O increases from the solar value, the relative abundance of atomic carbon will increase. For $\text{C/O} > 0.5$, the available atomic oxygen to form H_2O depends upon the CO/CH_4 ratio (Moses et al. 2013a), as most of the oxygen is locked in CO at high temperature, which is mostly the CO-dominated region, and the remaining available O forms H_2O . In that case, the H_2O abundance can deviate from the equilibrium abundance, and the quench level of H_2O can be used to determine the composition of the atmosphere.

4.4.2. CO_2

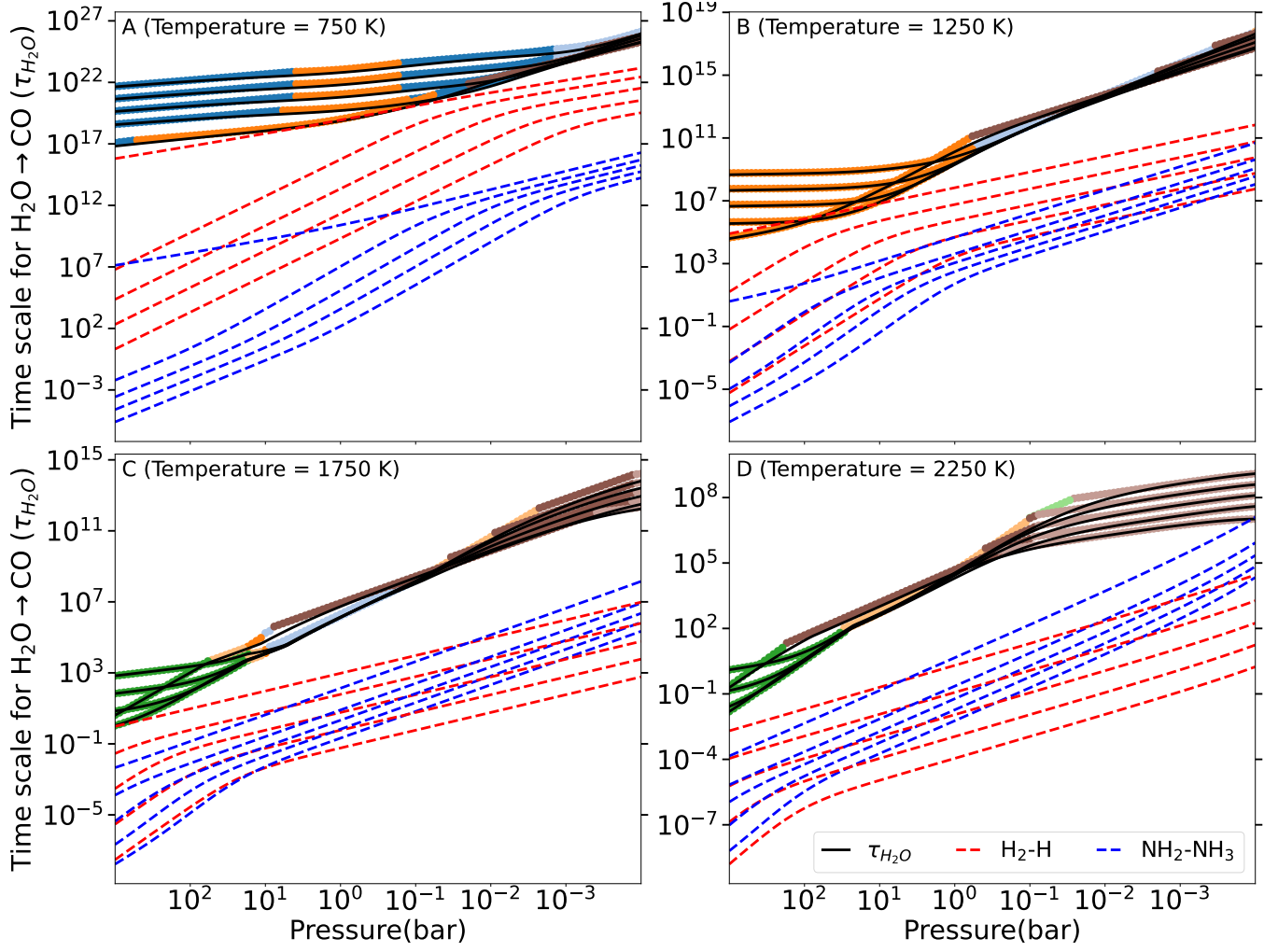
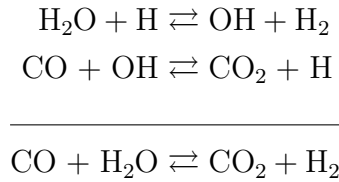


Figure 11. The timescale of conversion of $\text{H}_2\text{O} \rightarrow \text{CO}$ ($\tau_{\text{H}_2\text{O}}$) for four different temperatures (750 K, 1250 K, 1750 K, and 2250 K) with five different metallicities (0.1, 1, 10, 100, 1000 \times solar metallicity). The colored lines represent the timescale of RLS in corresponding temperature-pressure value from Figure 10, the red dashed lines represent $\tau_{\text{H}_2} \times \frac{3[\text{CO}]}{\text{H}_2}$ and the blue dashed represents $\tau_{\text{NH}_3} \times \frac{[\text{CO}]}{\text{NH}_3}$. The solid black line represents $\tau_{\text{H}_2\text{O}}$.

CO_2 recycles through H_2O and CO by a relatively fast conversion scheme (Line et al. 2010; Moses et al. 2011; Tsai et al. 2018).



The RLS for this conversion is the $\text{CO} + \text{OH} \rightleftharpoons \text{CO}_2 + \text{H}$ reaction. The $\text{CO} \rightleftharpoons \text{CO}_2$ conversion timescale is relatively fast compared to the $\text{CH}_4 \rightleftharpoons \text{CO}$ timescale. The RLS of $\text{CO} \rightarrow \text{CO}_2$ ($\text{CO} + \text{OH} \rightarrow \text{CO}_2 + \text{H}$) comes into the second type (both the reactants are heavy molecules), and

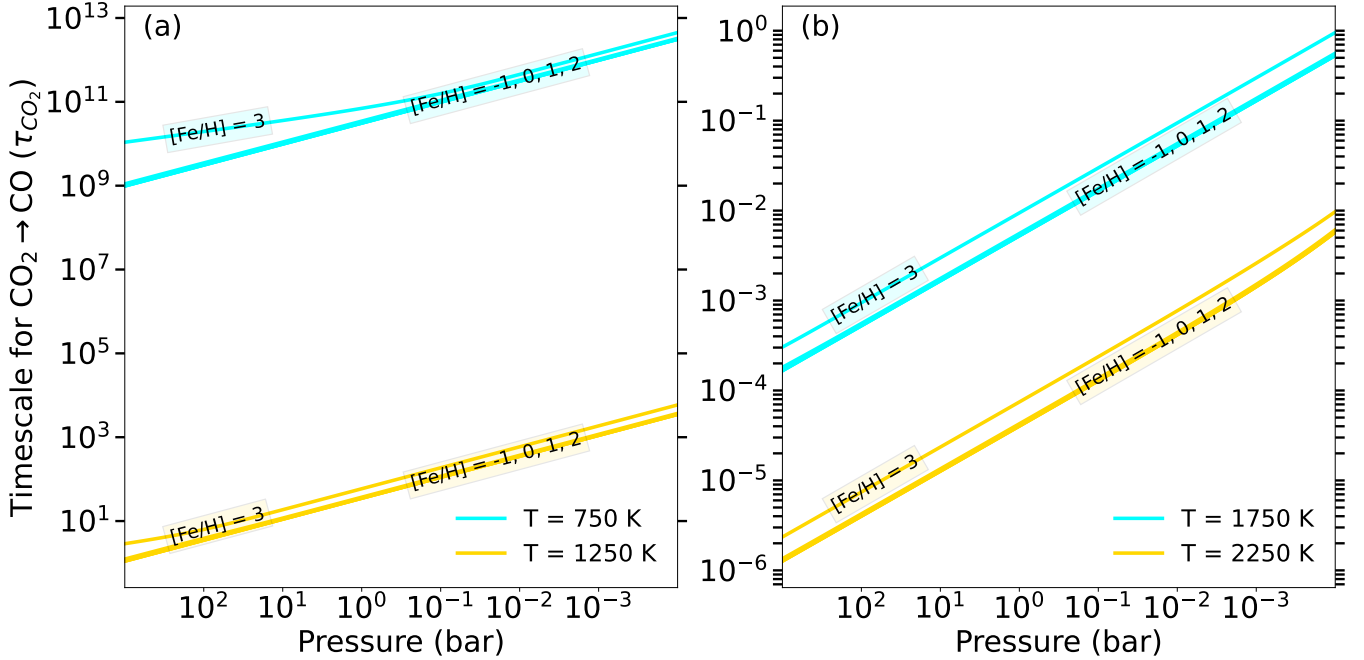


Figure 12. The timescale of conversion of $\text{CO}_2 \rightarrow \text{CO}$ ($\tau_{\text{H}_2\text{O}}$) for four different temperatures (750 K, 1250 K, 1750 K, and 2250 K) with five different metallicities (0.1, 1, 10, 100, 1000 \times solar metallicity). The colored lines represent the timescale of $\text{CO} \rightarrow \text{CO}_2$ for the labeled parameter.

the RLS of $\text{CO}_2 \rightarrow \text{CO}$ ($\text{CO}_2 + \text{H} \rightarrow \text{CO} + \text{OH}$) comes into the first type of RLS (H is one of the reactants). Thus, τ_{CO_2} increases with metallicity at a slow rate. In Figure 12, we have plotted τ_{CO_2} with pressure at different temperatures and metallicities. τ_{CO_2} is more than four orders of magnitude faster than τ_{CO} for 1750 K and 2250 K temperatures, and this difference drastically increases with the decreasing pressure. For 750 K, 1000 bar, and 0.1-100 \times solar metallicity, τ_{CO_2} is comparable to τ_{CO} , though for all the other parameter ranges, τ_{CO_2} is faster than τ_{CO} . The fast timescale of τ_{CO_2} makes the CO_2 abundance remain in equilibrium with H_2O and CO . Thus, for the pressure level, where CO follows its quenching abundance, CO_2 also deviates from its chemical equilibrium abundance. The chemical timescale of CO_2 increases with height. For a sufficiently high chemical timescale, the CO_2 abundance can be quenched at a high altitude where the CO_2 chemical timescale becomes comparable to the vertical mixing timescale. However, the quenched CO_2 abundance does not contribute to the infrared part of the transmission or emission spectra of the planets because the infrared spectrum is shaped well below the CO_2 quench level ($P > 10^{-4}$ bar) (Moses et al. 2011).

5. APPLYING ON THE TEST EXOPLANETS

The quenching approximation has the potential to constrain the disequilibrium abundance. Here, we have benchmarked the quenching approximation results with the photochemistry-transport model (described in Section 2 and Appendix). For the benchmarking, we used two exoplanets, namely HD 189733 b and GJ 1214 b. HD 189733 b is a gas giant with an orbital period of 2.22 days (Moutou et al. 2006), and GJ 1214 b is a Neptune-sized planet with an orbital period of 1.58 days (Charbonneau et al. 2009). These two exoplanets are excellent candidates for this study since their equilibrium temperature is such that it intersects the CH_4 - CO boundary at 10 bar and 10^{-5} bar pressure which leads to having a more pronounced effect of the transport on CH_4 and CO abundances. HD 189733

Table 1. Parameters for the exoplanets studied

Name	[Fe/H]	C/O	Intrinsic temperature	Heat redistribution	Reference
HD 189733 b	0	Solar	-	No redistribution	Moses et al. (2011)
GJ 1214 b	2	Solar	60 K	Equal redistribution	Charnay et al. (2015)
HR 8799 b	0	0.66	-	-	Moses et al. (2016)
GJ 436 b	-	1	-	-	Line et al. (2014)
WASP-39 b	1	0.35	-	Equal redistribution	Tsai et al. (2022); The JWST Transiting Exoplanet Community Early Release Science Team et al. (2022)

b and GJ 1214 b have $T_{eq} \approx 1200$ K and 600 K, and surface gravity $g_{surface} \approx 21.5$ m s⁻² and 8.9 m s⁻² respectively. To find the quench level of CH₄ and CO, we overplotted the T-P profile of HD 189733 b and GJ 1214 b with the constant contour of the quench level (given in Figure 9) for assorted metallicities. Using the quench level, we found the quenched abundance and benchmarked it with the photochemistry-transport model. For the benchmarking, we turned off the photochemistry and molecular diffusion for the photochemistry-transport model since the quenching approximation only deals with the Eddy diffusion. However, molecular diffusion and photochemistry can affect our results, depending upon the strength of the stellar radiation at the top of the atmosphere and the strength of transport. For moderate values of the Eddy diffusion coefficient (10⁶-10⁹ cm² s⁻¹), Eddy diffusion dominates over molecular diffusion in the parameter range we considered. As described in Hu and Seager (2014), the homopause (the pressure level where both the coefficients become equal) is at 10⁻⁵ bar for $K_{zz} = 10^6$ cm² s⁻¹ for GJ 1214 b. The photochemical products formed at high altitudes can diffuse in the deep atmosphere and change the composition. As discussed in Moses et al. (2011) and Madhusudhan et al. (2016), the photochemical products can reach up to 10⁻⁴ bar for high radiated hot Jupiter. However, photochemical products can affect the atmospheric composition of a lower-temperature atmosphere.

5.1. HD 189733 b

The T-P profile for HD 189733 b is adopted from Moses et al. (2011) (see Table 1 for parameters) and overplotted with the contours of the quench level of CO and CH₄ in Figures 13 (a) and (b) respectively. The T-P profile crosses the CH₄-CO boundary at the 10 bar pressure level for solar metallicity. The temperature is warm enough to make CO the dominant species. Below 10 bar, CH₄ is the dominant C-bearing species, and above 10 bar, CO becomes the primary C-bearing species. Figures 13 (c) and (d) show the mixing ratio of CO and CH₄ respectively for 20 different metallicities. With increasing metallicity, the CH₄-CO boundary moves towards the high-pressure and low-temperature region, shifting a greater part of the thermal profile into the CO region. The CO equilibrium abundance increases for the entire pressure range as the metallicity increases. However, the CH₄ equilibrium abundance first increases and then decreases with increasing metallicity in the high-pressure region, and in the low-pressure region, the abundance decreases with the increasing metallicity. The quench level of CO lies well below the CH₄ quench level. CO is the dominant species at the CO quench level, making CO the major source of carbon in the transport-dominated atmosphere. Increasing metallicity does not alter the dominant C-bearing species; as the metallicity increases, CO becomes more abundant. The CO quench level shifts towards the high-pressure region,

increasing the mixing ratio of CO in the transport-dominated region with metallicity. Also, CO_2 and H_2O follow the equilibrium abundance.

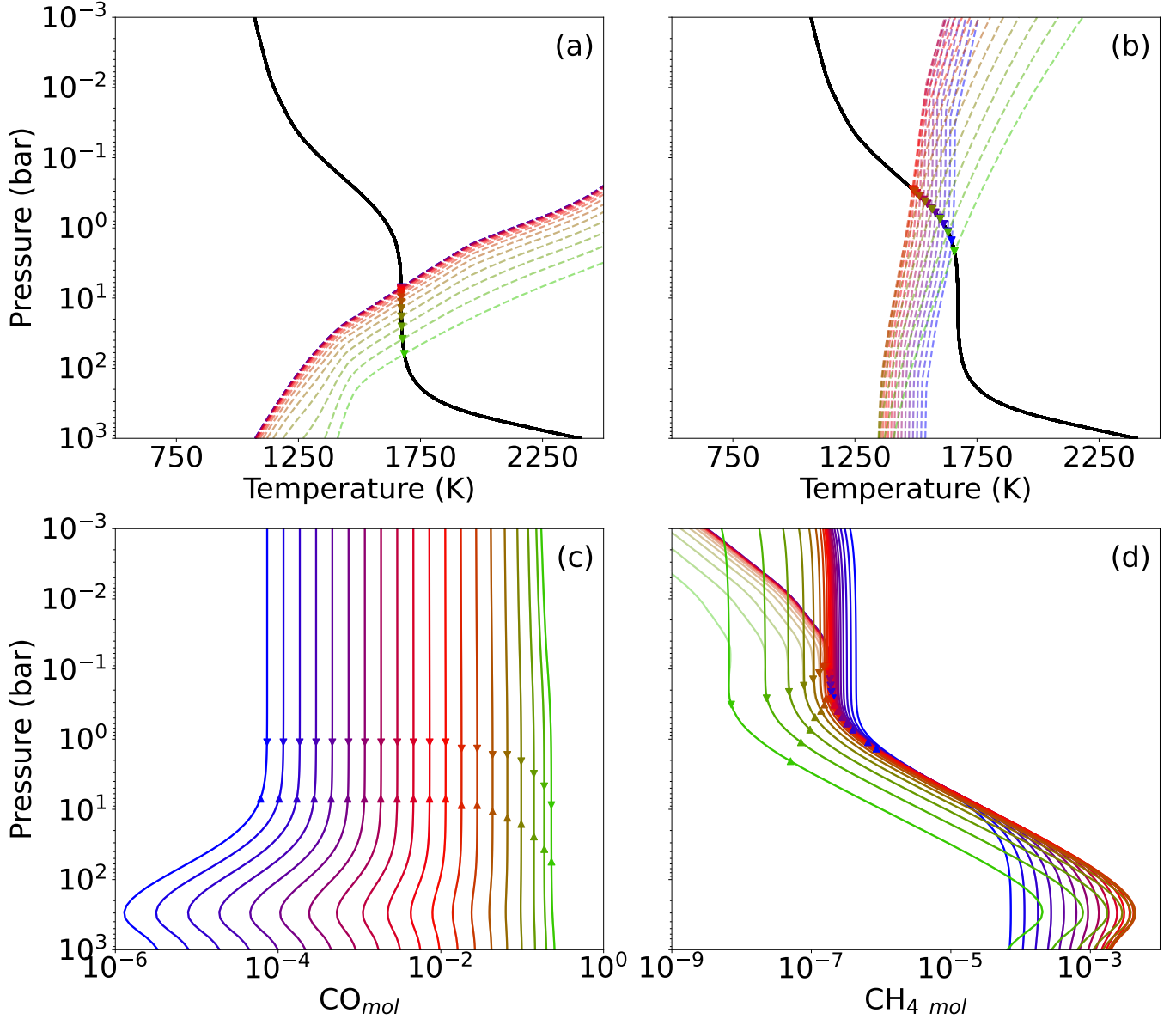


Figure 13. The top panel shows the T-P profile overplotted with the quenched curve of (a) CO and (b) CH_4 for 20 different metallicities (blue-red-green lines are from 0.1-10-1000 \times solar metallicity). The quench level contour is calculated for the $K_{zz} = 10^9 \text{ cm}^2 \text{ s}^{-1}$ and assuming the mixing length is equal to $0.1 \times$ atmospheric scale height. The bottom panel shows the mixing ratio of (c) CO and (d) CH_4 , for the same set of metallicities. The colored lines are the output of the photochemistry-transport model and the corresponding faded colored lines are the equilibrium abundances. The upper and lower triangles are the quench levels calculated using $0.1H$ and $1H$ as the mixing length.

Figure 14 shows the T-P profile of GJ 1214 b (see Table 1 for parameters), overplotted with the contours of the quench level of (a) CO and (b) CH₄. The T-P profile is adopted from Charnay et al. (2015), and for solar [Fe/H], it crosses the CH₄–CO boundary at 10⁻⁵ bar pressure level. The temperature is sufficiently low to make CH₄ the dominant C-bearing species at solar metallicity. However, as the metallicity increases, the equal-abundance curve of CH₄–CO moves towards low temperature, and as a result, the region where the T-P profile lies changes from CH₄ to CO dominant region. In the transport-dominated region and $P < 50$ bar, CH₄ remains the dominant C-bearing species for [Fe/H] < 100× solar metallicity. For $P > 50$ bar, CH₄ dominates over CO for [Fe/H] < 30× solar metallicity. In Figures 14 (c) and (d), the mixing ratio of CO and CH₄ for 20 different metallicities are shown. The quench level of CO and CH₄ lies at 10² bar pressure level; the temperature determines whether CO or CH₄ will dominate in the transport region. As the metallicity increases, the CO equilibrium abundance increases for the entire pressure range. However, the CH₄ equilibrium abundance shows complex behavior with metallicity. For $P < 10^2$ bar and metallicity < 600 × solar metallicity, the CH₄ abundance increases with increasing metallicity, and for metallicity > 600 × solar metallicity, the CH₄ abundance starts to decrease, and CO starts to become the major C-bearing source.

5.3. Quench level analysis on the test exoplanets

It is apparent that CH₄ and CO can quench at different pressure levels depending on the thermal profile. In the equilibrium composition, τ_{CH_4} and τ_{CO} become equal at the equal-abundance curve. If the T-P profile intersects the equal-abundance curve, say at a pressure level P_i and the atmospheric mixing is such that the quench level lies close to P_i , then CH₄ and CO can quench at the same pressure level. If the quench level lies well below/above the P_i pressure level, they can quench at different atmospheric heights. We can find which species quench first by tracing the equal abundance and thermal profile. In Figure 9(b), it is shown that for a fixed metallicity and K_{zz} value, the CO quenched curve is at a higher temperature relative to the CH₄ quenched curve in the CO dominated region, and the CH₄ quenched curve is at a higher temperature in the CH₄ dominated region. Along with this, assuming the temperature is decreasing with decreasing pressure (no thermal inversion) or remains isothermal, then in the CO dominated region (right side of the equal-abundance curve), CO will quench first, and in the CH₄ dominated the region, CH₄ quenches first.

We used two extreme values, i.e., $0.1 \times H$ and $1 \times H$ as the mixing length and calculated the quenched abundances instead of using the method given in Smith (1998) to find the mixing length. As evident from Figures 13 and 14, all the modeled transport abundances (mixing ratio from full chemical kinetics model) lie in between the quenched abundances with mixing length $L = 0.1 \times H$ and $1 \times H$. We define the error as the difference between the maximum and minimum equilibrium abundances between $P_{0.1}$ and P_1 , where $P_{0.1}$ is the quench pressure given by $L = 0.1 \times H$ and P_1 is the quench pressure given by $L = 1 \times H$. For HD 189733 b, the CO abundance is accurate within \approx a factor of two for low metallicity and matches with the chemical kinetics model for high metallicity. The reason for the good agreement of quenching approximation and chemical kinetics model for CO is that the equilibrium mixing ratio of CO does not change with pressure. As a result, the quenched abundance of CO becomes independent of transport. However, for CH₄, the accuracy is within \approx an order of magnitude. For GJ 1214 b, the CO abundance is accurate within \approx a factor of five for low metallicity and within \approx a factor of two for high metallicity. For CH₄, it is accurate within \approx a factor of two and seven for low and high metallicity, respectively. The quenching accuracy depends upon the pressure difference between the quench pressure with $L = 0.1 \times H$ and $1 \times H$ and the change of

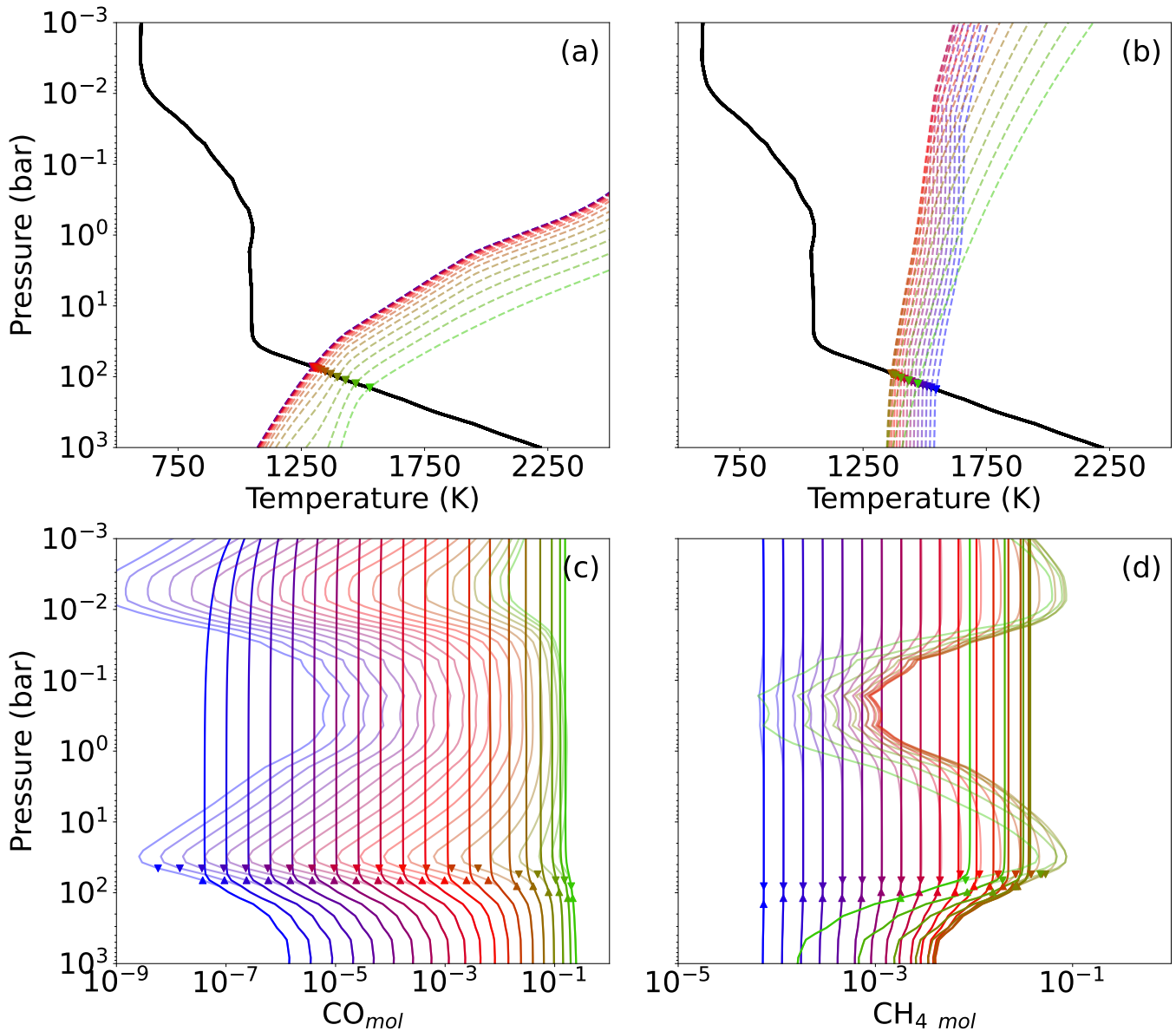


Figure 14. Same as Figure 13, but for GJ 1214 b

the equilibrium abundance between these pressure levels. As metallicity affects both these quantities, the accuracy of the quenching approximation is changed with metallicity. Also, the metallicity effect on the quenching approximation differs for different molecules and T-P profiles. For GJ 1214 b, the increment of metallicity improves the quenching accuracy for CO while decreasing it for CH_4 .

5.4. Constraint on Metallicity and Transport Strength

The quenching approximation is a powerful tool that can constrain the metallicity and transport strength without solving the photochemistry-transport model. To constrain the metallicity and transport strength, the observed abundance of molecules and the thermal profiles of the exoplanets are overplotted with the color-mesh plot of the equilibrium mixing ratio and quenched curve of the molecules (see Figures 15-18).

To demonstrate this fact, we use four case studies. We chose HR 8799 b as our first case study; it is a gas giant with $7 M_J$ mass and $1.2 R_J$ radius, which was discovered by direct imaging (Marois et al. 2008). For the second and third cases, we take GJ 436 b and the previously mentioned exoplanet HD 189733 b. GJ 436 b is a Neptune-sized exoplanet with a 2.6 days orbital period, discovered in 2004 (Bailey et al. 2004) and having a high C/O ratio ≈ 1 , whereas HR 8799 b has C/O ≈ 0.66 (Line et al. 2014; Barman et al. 2015).

- We overplotted the observed CH_4 ($10^{-6} < \text{CH}_4$ mole fraction $< 10^{-5}$) and CO ($10^{-4} < \text{CO}$ mole fraction $< 3 \times 10^{-4}$) abundance of HR 8799 b (T-P profile taken from Moses et al. (2016), see Table 1 for parameters) with the quenched curve in the equilibrium abundance data in Figures 15 and 16. The observed abundance is taken from Barman et al. (2015). The region between the solid blue lines marks the observed abundance for CH_4 . It can be seen that the T-P profile cuts this region for all four metallicities, but the corresponding $\log_{10}(K_{zz})$ value lies between 7 and 10. Therefore, CH_4 cannot constrain the metallicity value but provides the K_{zz} value. When we examine the observed CO abundance, it can only be constrained by the solar metallicity (see Figure 16). Since a large part of the T-P profile lies in the CO dominated region, it cannot constrain K_{zz} ; in fact all the K_{zz} values are possible. Also, for the subsolar metallicity, the CO abundance is very low ($\text{CO}_{mix} = 10^{-5}$) throughout the thermal profile. For the supersolar metallicity, the quench level to achieve observational CO abundance ($\text{CO}_{mix} \approx 10^{-4}$) lies in low-temperature and high-pressure regions, which require low internal temperature. Simultaneous constrain on the observed CH_4 and CO abundance conclude that the solar metallicity can explain the abundance along with $K_{zz} = 10^7$ to $10^{10} \text{ cm}^2 \text{ s}^{-1}$. The same conclusion has been made by Moses et al. (2016) with a kinetic/transport model. They use $K_{zz} = 4 \times 10^7 \text{ cm}^2 \text{ s}^{-1}$, the solar metallicity, and C/O = 0.66 to best fit the observed abundance.
- In the second case, we took GJ 436 b (T-P profile taken from Line et al. (2014), see Table 1 for parameters), and overplotted the observed CH_4 ($10^{-9} < \text{CH}_4$ mole fraction $< 10^{-8}$) and CO ($3.4 \times 10^{-3} \approx \text{CO}$ mole fraction) abundance with the quenched curve in the equilibrium abundance data in Figures 17 and 18. The observed CH_4 abundance cannot be achieved from the parameter range used in this study. However, the CO abundance can be achieved for high metallicity ($> 100\times$ solar), which is also concluded in Line et al. (2014). It is to be noted that the current study only focuses on the solar C/O ratio; therefore, it is unable to explain the CH_4 abundance. The super-solar C/O ratio is required to reach the observed CH_4 abundance, as increasing the C/O ratio shifts the CH_4 -CO boundary towards lower pressure and higher temperature.
- In the third case, we took HD 189733 b and overplotted the observed CH_4 ($10^{-5} < \text{CH}_4$ mole fraction $< 2 \times 10^{-5}$) and CO ($2 \times 10^{-5} < \text{CO}$ mole fraction $< 3 \times 10^{-2}$) abundances with the quenched curve in the equilibrium abundance data in Figures 19 and 20. The observed abundance is adopted from Line et al. (2014). We find that high transport ($K_{zz} > 10^{10} \text{ cm}^2 \text{ s}^{-1}$) along with $0.1\text{-}10 \times$ solar metallicity can constrain the observed CH_4 and CO abundances.
- WASP-39 b is among the first exoplanets whose atmosphere has been constrained by JWST, and its observed atmospheric metallicity is found to be $[\text{Fe}/\text{H}] = 1$ (Tsai et al. 2022; The

JWST Transiting Exoplanet Community Early Release Science Team et al. 2022; Rustamkulov et al. 2022). We constrained the quenched abundance of CH_4 and CO for various vertical mixing strengths for WASP-39 b. In Figures 21 and 22, we have plotted the thermal profile of WASP-39 b and the quenched curve on the equilibrium data of CH_4 and CO . The thermal profile is taken from Tsai et al. (2022) (see Table 1 for parameters), and The JWST Transiting Exoplanet Community Early Release Science Team et al. (2022). We find that the CH_4 and CO mixing ratios are independent of vertical mixing for $K_{zz} < 10^{10} \text{ cm}^2 \text{ s}^{-1}$, since the part of the thermal profile where quenching of CH_4 takes place remains close to the contour of $\text{CH}_4 \sim 10^{-7}$ mixing ratio. For high vertical mixing $K_{zz} > 10^{10} \text{ cm}^2 \text{ s}^{-1}$, the quenched CH_4 mixing ratio can increase by one order of magnitude. For $[\text{Fe}/\text{H}] = 1$, the thermal profile lies in the CO dominated region, and the CO mixing ratio for all vertical mixing is 4×10^{-3} . CO remains in equilibrium, and H_2O is the dominant species of O for the solar C/O ratio when $[\text{Fe}/\text{H}] = 1$ (i.e., $10 \times$ solar metallicity), and CO_2 remains in equilibrium with CO and H_2O . This makes sure that CO , CO_2 , and H_2O are independent of vertical mixing and remain in equilibrium for WASP-39 b. In Figure 23, we have shown the equilibrium mixing ratios of CO , CO_2 , and H_2O for 0.1, 1, 10, and $100 \times$ solar metallicity. The CO_2 , H_2O , and CO abundance profiles for $10 \times$ solar metallicity are qualitatively similar to the retrieved abundance from The JWST Transiting Exoplanet Community Early Release Science Team et al. (2022).

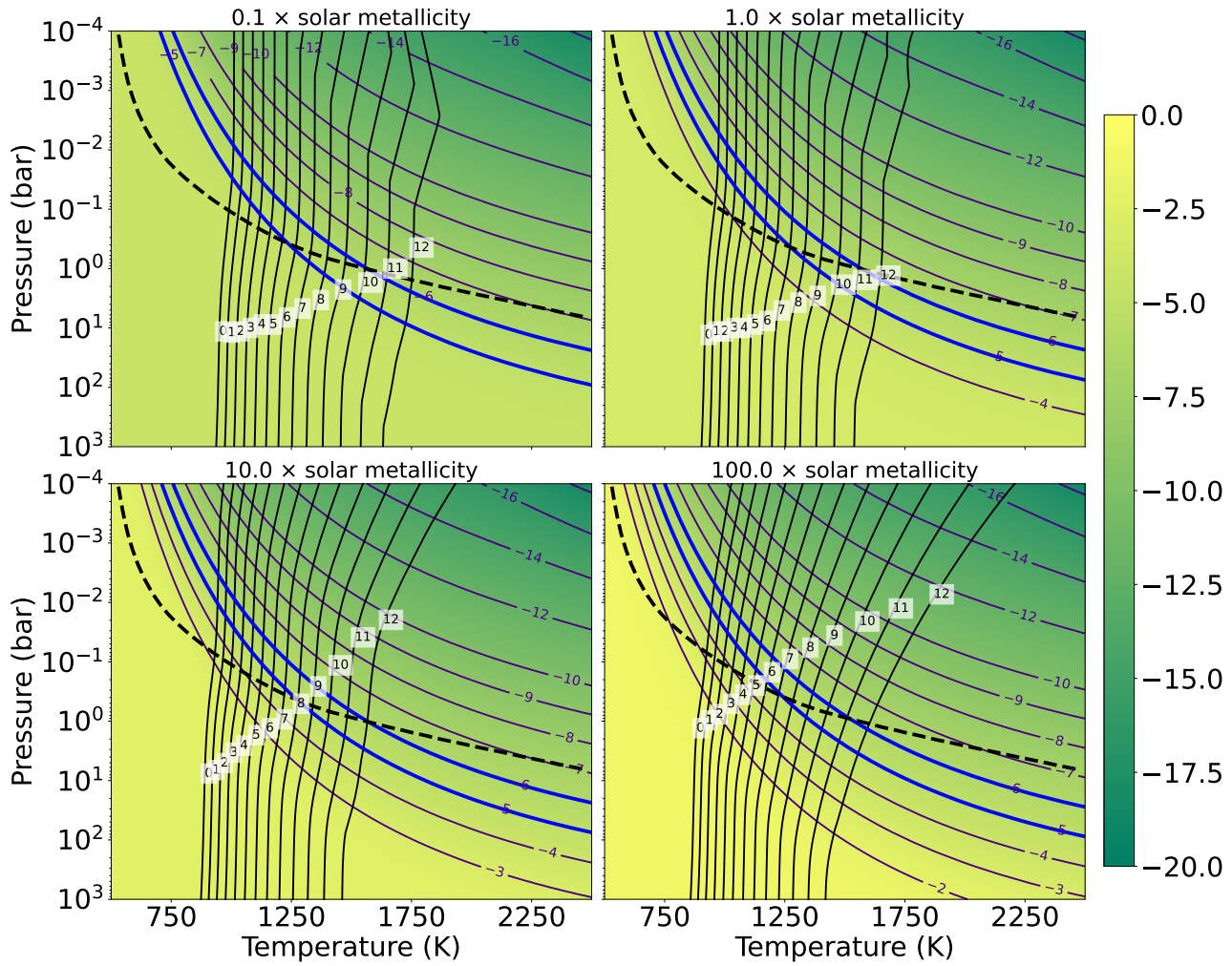


Figure 15. The color bar shows the mole fraction of CH_4 in the log10 scale as a function of pressure and temperature. The region between the solid blue lines are the observational constrain of HR 8799 b taken from Barman et al. (2015), the black dashed line is the T-P profile adopted for $T_{eff} = 1000$ K and $g = 3000$ cm s^{-2} , which is adopted from Moses et al. (2016). The solid black lines are the quench lines for different K_{zz} values (label in the plots). The four panels represent the different values of atmospheric metallicity.

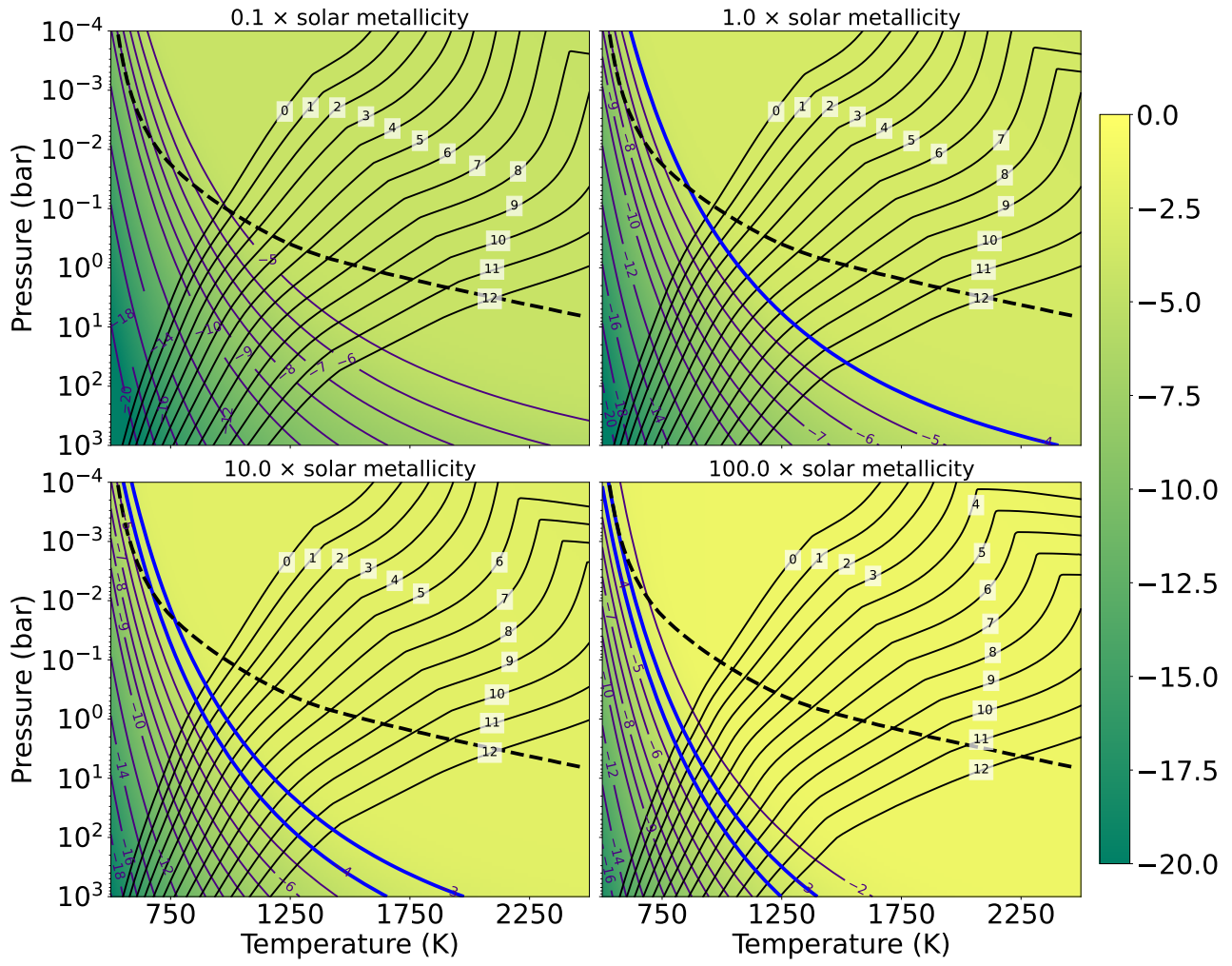


Figure 16. Same as Figure 15, but for CO (for HR 8799 b).

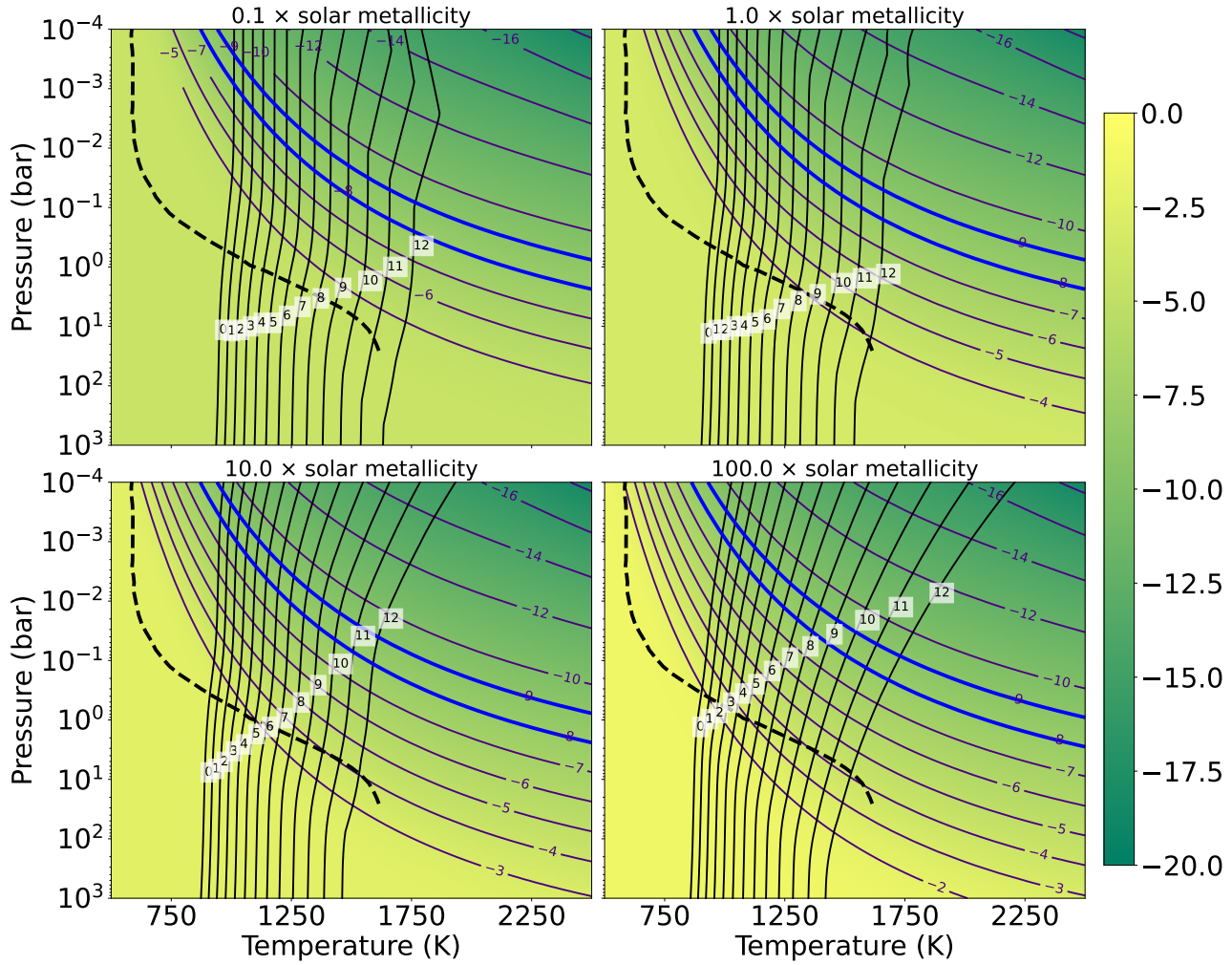


Figure 17. The colour bar shows the equilibrium mole fraction of CH_4 in the log10 scale as a function of pressure and temperature. Along with the color bar, the contour of constant mixing ratio also plotted. The region between the solid royal-blue lines are the observational constrain of the GJ 436 b taken from [Line et al. \(2014\)](#), the black dashed line is the T-P profile adopted from [Line et al. \(2014\)](#). The solid black lines are the quench lines for different K_{zz} values (label in the plots). The four panels represent the different values of atmospheric metallicity

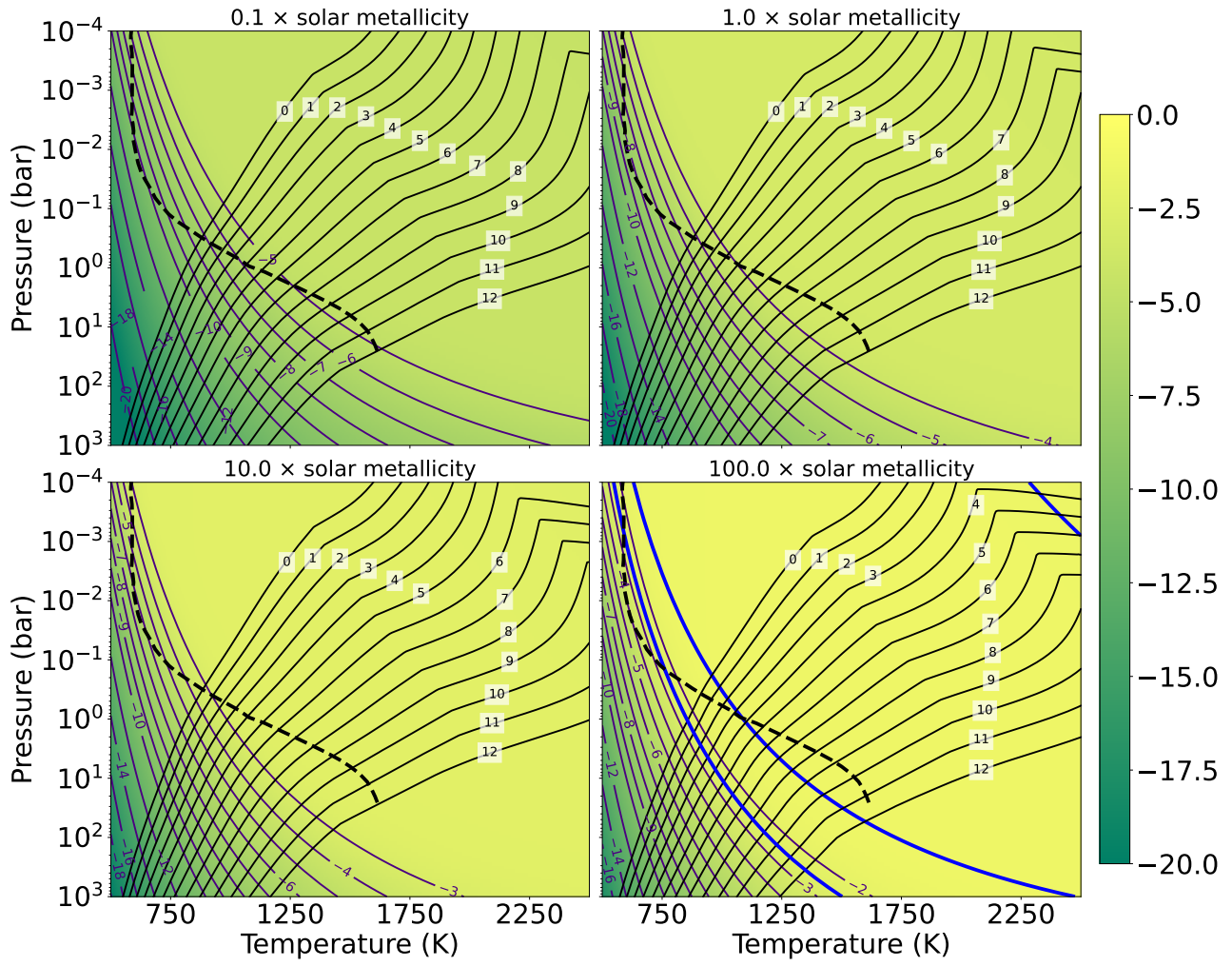


Figure 18. Same as Figure 17, but for CO (for GJ 436 b). For visualization, the royal-blue curve are at 10^{-4} and 10^{-3} contour of equilibrium mixing ratio.

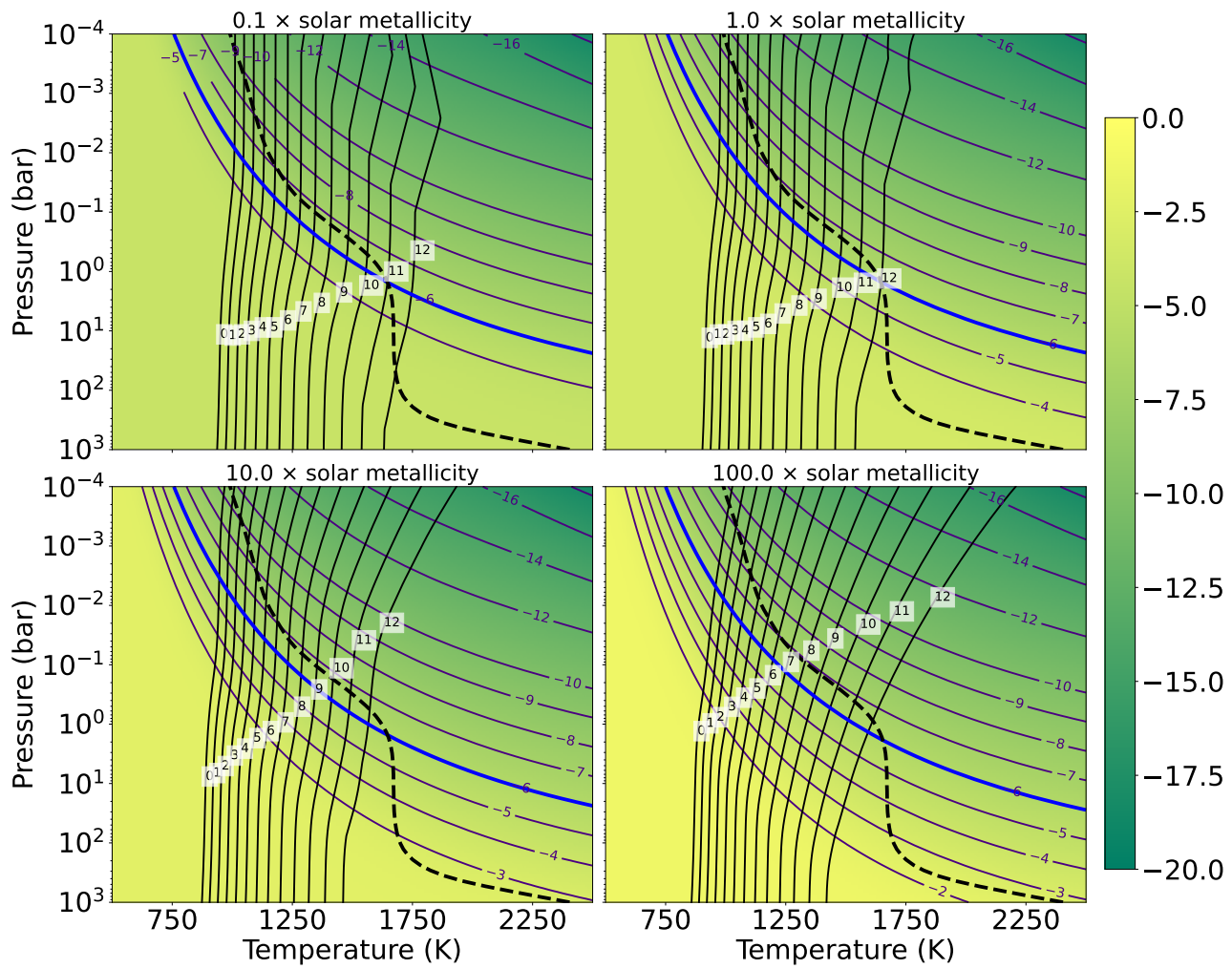


Figure 19. Same as Figure 17, but for HD 189733 b with CH_4 .

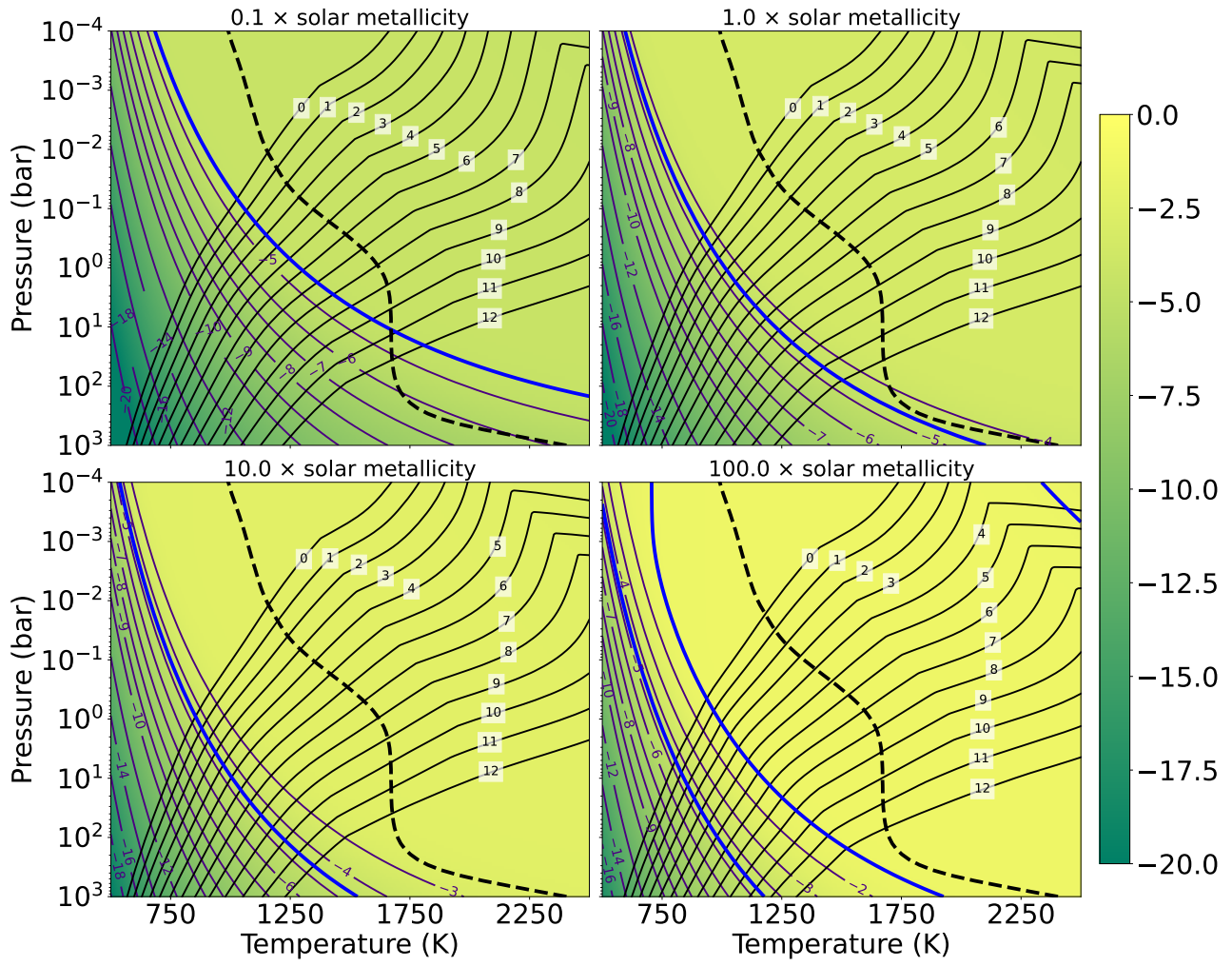


Figure 20. Same as Figure 17, but for HD 189733 b with CO.

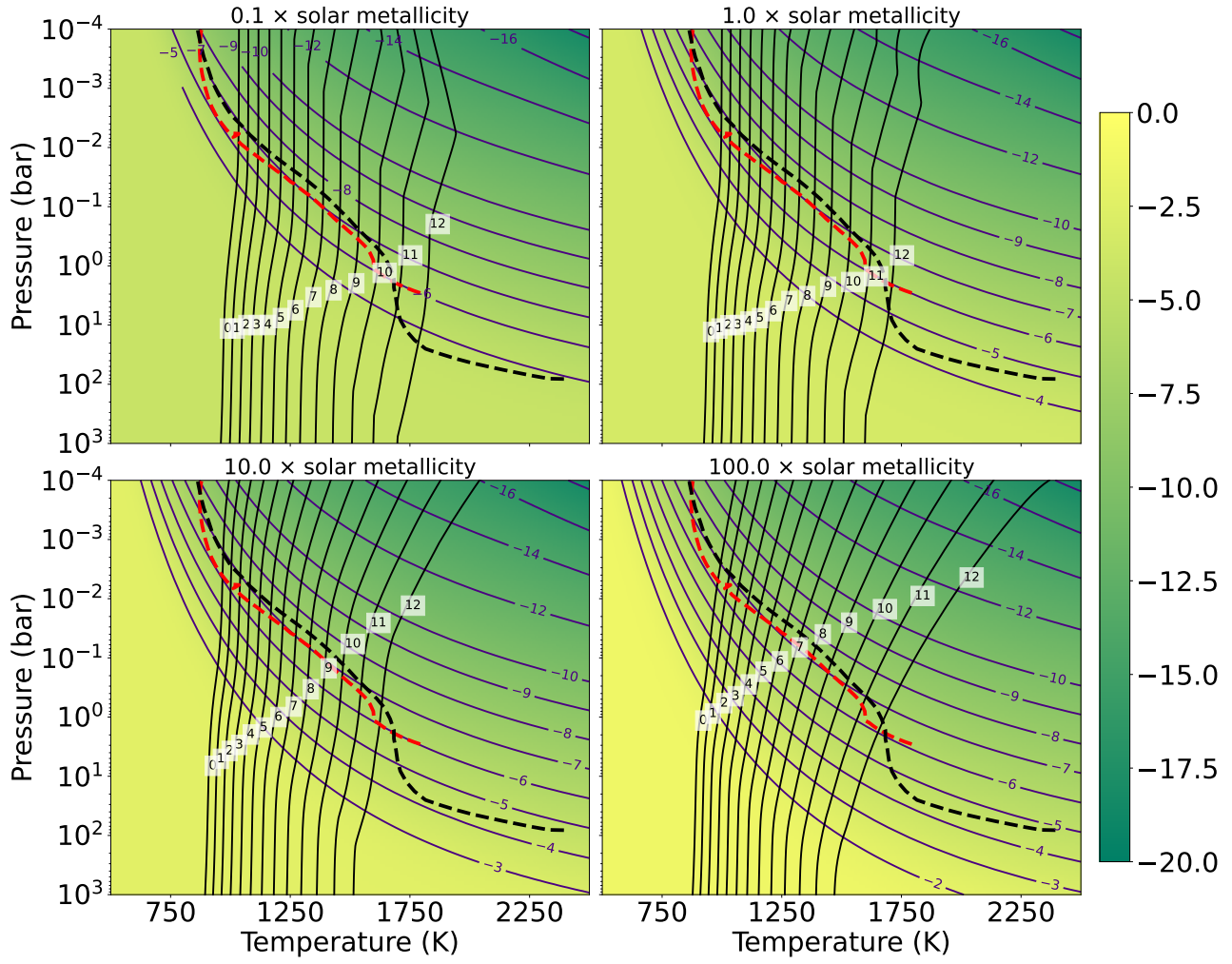


Figure 21. The colour bar shows the equilibrium mole fraction of CH_4 in the log10 scale as a function of pressure and temperature for WASP-39 b. Along with the color bar, the contours of constant mixing ratio are also plotted. The T-P profiles are shown in black dashed and red dashed lines, and are taken from [The JWST Transiting Exoplanet Community Early Release Science Team et al. \(2022\)](#) and [Tsai et al. \(2022\)](#) respectively. The solid black lines are the quench lines for different K_{zz} values (label in the plots). The four panels represent the different values of atmospheric metallicity.

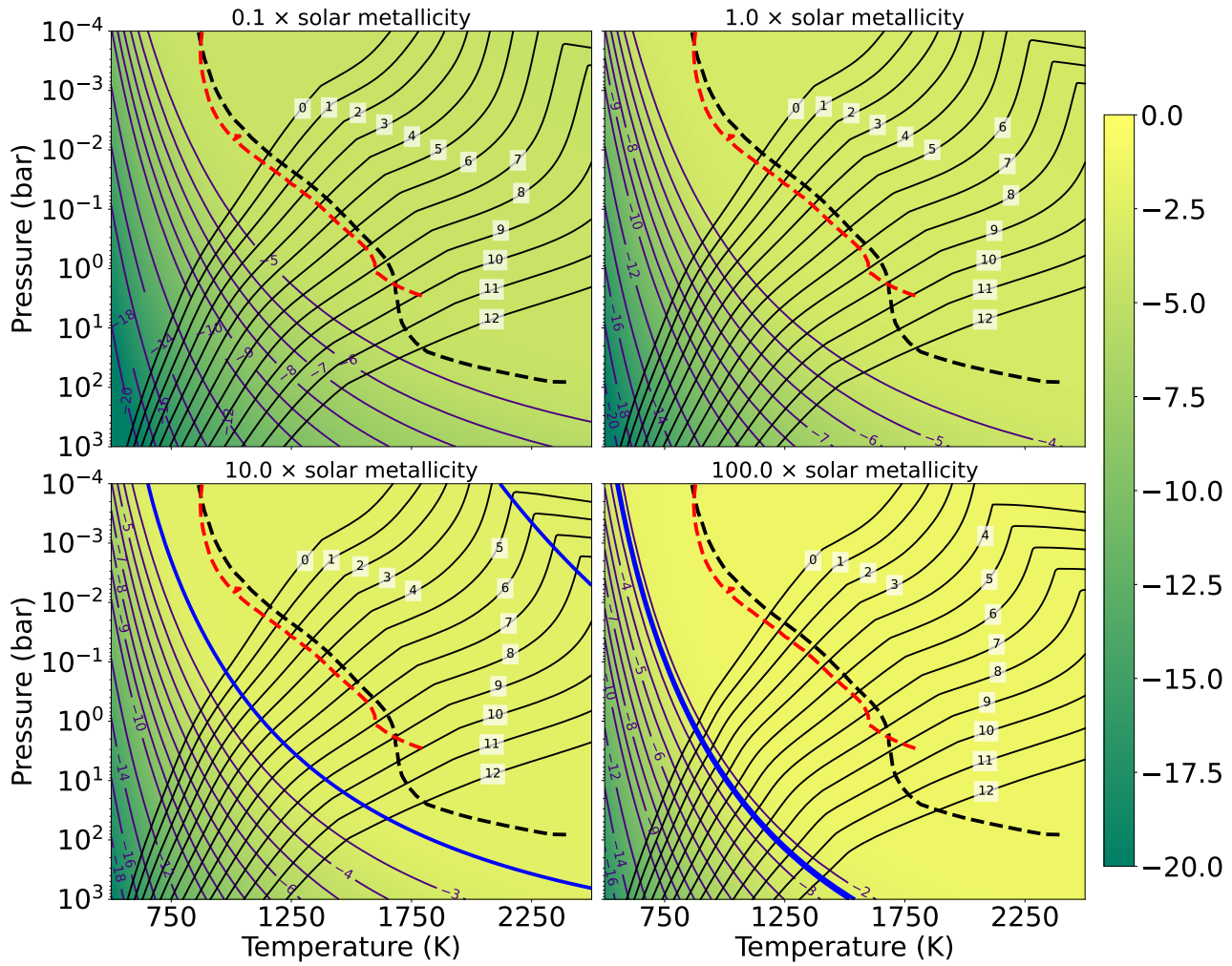


Figure 22. Same as Figure 21, but for CO (for WASP-39 b). Here, blue lines represent the equilibrium mixing ratio contours of 4×10^{-3} and 5×10^{-3} .

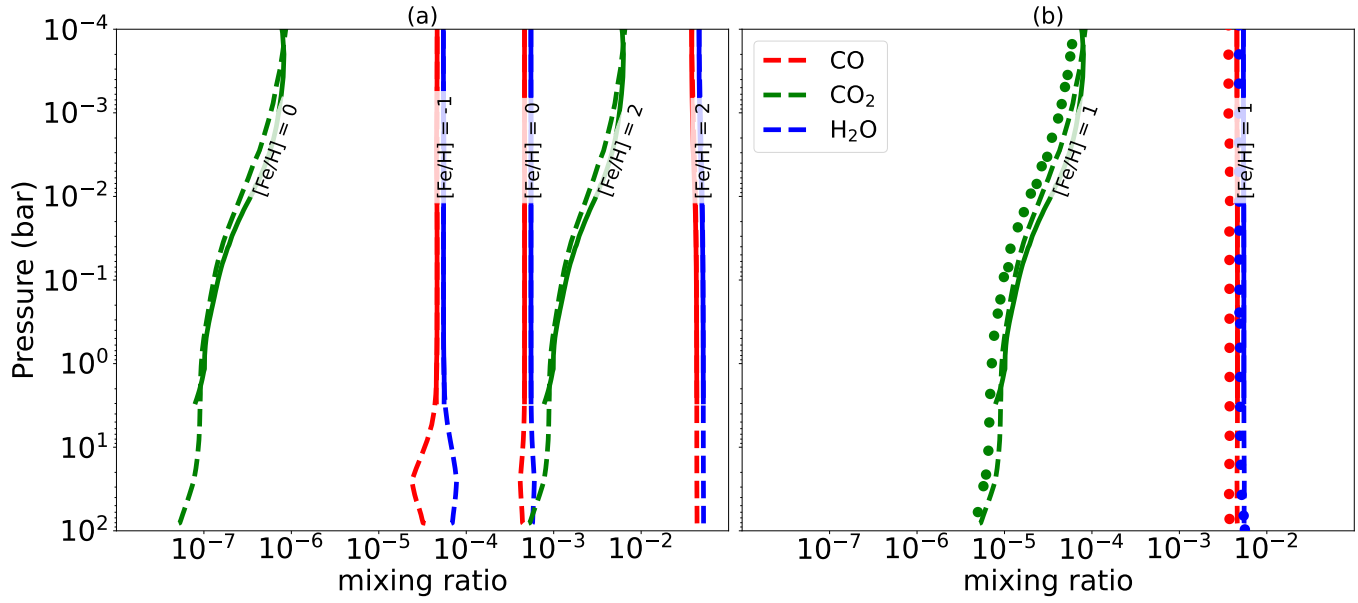


Figure 23. The equilibrium abundances of CO₂, CO and H₂O for two different T-P profiles of WASP-39 b (dashed: The JWST Transiting Exoplanet Community Early Release Science Team et al. (2022) and solid: Tsai et al. (2022)) are shown for metallicity (a) $[\text{Fe}/\text{H}] = [-1, 0, 2]$ and (b) $[\text{Fe}/\text{H}] = [1]$. The colored circles in panel (b) are the abundances taken from The JWST Transiting Exoplanet Community Early Release Science Team et al. (2022).

5.5. Comparison with analytical expressions for chemical timescale

We compare the chemical timescale from our model with Zahnle and Marley (2014), in which authors provided analytical expressions for the chemical timescale to calculate the quenched pressure and temperature. Their analytical expressions applied to self-luminous exoplanets and they assumed the mixing length to be $1 \times H$. In Figure 24, we have compared the chemical timescale from both the studies. We have taken the thermal profile (black solid line) from Zahnle and Marley (2014) for $T_{eff} = 600$ K and $g = 10^3$ cm s⁻². The chemical timescales from our model deviate significantly from Zahnle and Marley (2014) in the low-temperature and high-pressure region for CH₄ and H₂O, and in the low-pressure and low-temperature region for CO. The green patch in Figure 25 highlights the region where our results are in agreement with Zahnle and Marley (2014). It is to be noted that temperature falls very rapidly with pressure in the region where the quench level lies. The chemical timescale is a strong function of temperature; as a result, the deviation of a few orders of magnitude in the chemical timescale only shifts the quench level by a few factors in the pressure scale. The resulting change in the CH₄ or CO mixing ratios can be small. The thermal profile remains close to the contour of (CH₄/CO), change of the chemical timescale by a few orders of magnitude does not change the CH₄ or CO mixing ratio significantly. It is clear from Figure 5 of Zahnle and Marley (2014) that the authors did not consider K_{zz} below 10^4 cm² s⁻¹ and therefore, they did not get the quenched temperature below 1000 K. Thus, extrapolating the analytical expression for $T < 1000$ K can give erroneous results as is evident in Figure 25.

6. DISCUSSION

6.1. CH₄ Depletion

In the solar system, methane is observed in all the giant planets, and its formation can be explained with the low-temperature chemistry (Guillot 1999). In the exoplanet atmosphere, methane is found to be depleted and observed only in a few exoplanets (Madhusudhan 2019; Molaverdikhani et al. 2020). The methane depletion can be related to the presence of the disequilibrium processes; Molaverdikhani et al. (2019) found that strong vertical mixing can increase or decrease the methane abundance in the atmosphere. Depletion of methane can also result from the presence of clouds that heat the atmosphere and make methane less dominant (Molaverdikhani et al. 2020) and the photochemistry can also deplete methane in the photochemical region of the atmosphere ($P < 0.1$ mbar). In this section, we discuss the possibility of methane depletion in the presence of vertical mixing.

- As discussed in Section 4.1, the abundance of methane increases with metallicity only at the high-pressure and low-temperature region where methane is the dominant species of carbon. CH₄ remains constant with metallicity in the high-temperature and low-pressure region where CO is the dominant C-bearing species. As metallicity is increased, the CO abundance first increases linearly at the high-temperature region, and the metallicity dependence gets stronger with decreasing temperature. Thus, increasing metallicity decreases the relative abundance of CH₄, so in a high metallicity atmosphere, CH₄ can be depleted.
- Vertical mixing can support the low methane abundance. In Figure 9, for most of the temperature-pressure range, the CO quench level lies well below the CH₄ quench level. Thus CO is quenched in high-temperature and high-pressure regions of the atmosphere. In contrast, CH₄ is quenched in the low-temperature region.

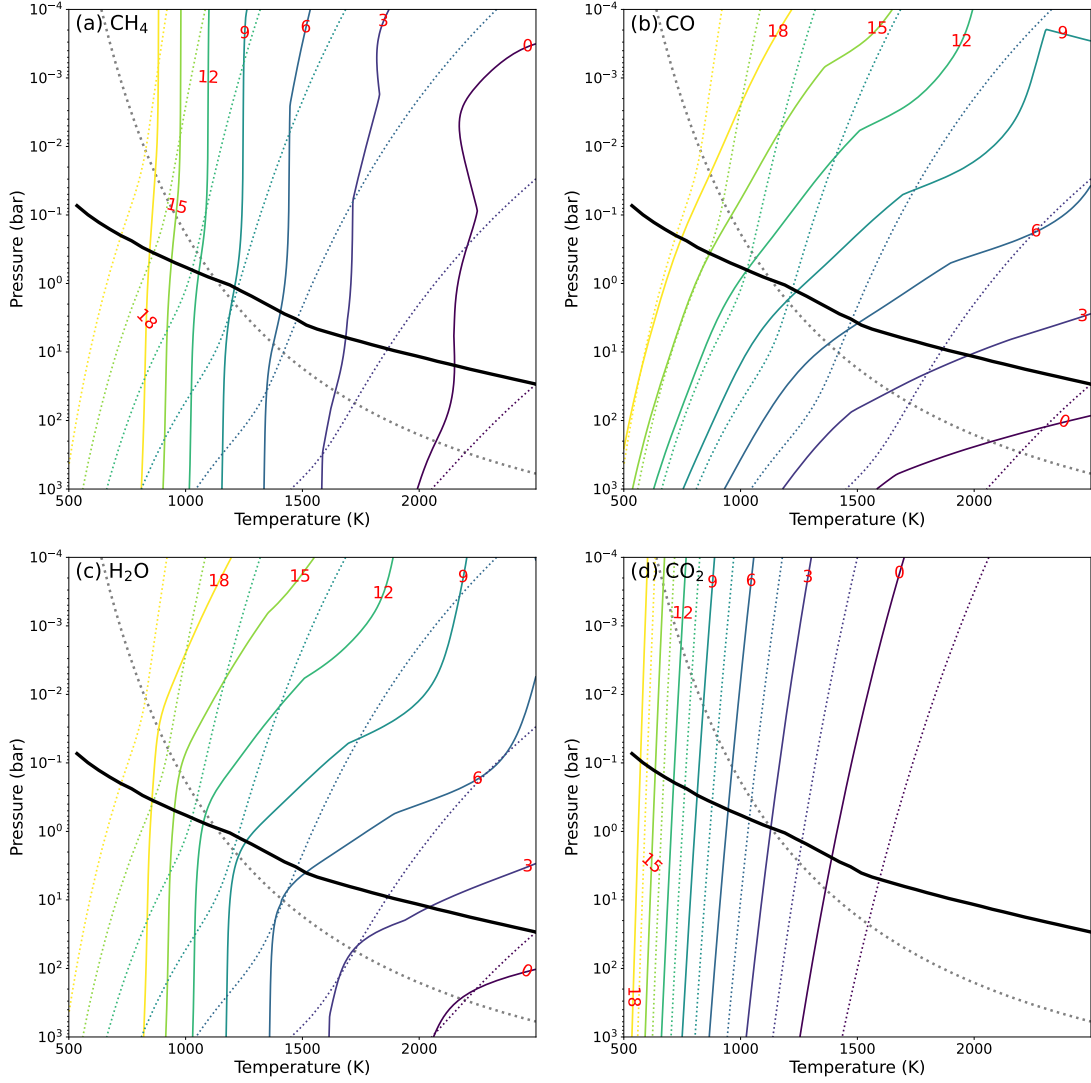


Figure 24. The contours of the chemical timescales of (a) CH_4 , (b) CO, (c) H_2O , and (d) CO_2 obtained from our study (denoted by the colored solid lines) along with the timescales computed from the analytical expression from Zahnle and Marley (2014) are shown in the log10 scale. The black dotted line represents the equal-abundance curve of CH_4 -CO and the black solid line is the T-P profile taken from Zahnle and Marley (2014) for $T_{\text{eff}} = 600$ K and $g = 10^3$ cm s $^{-2}$.

- As shown in §4 of Zahnle and Marley (2014), the CH_4 -CO boundary is always shallower than the adiabatic T-P profile. This suggests that the adiabatic T-P profile lies in the CH_4 region for low internal temperature exoplanets. The adiabatic T-P profile intersects the CH_4 -CO boundary for high internal temperature. In the high internal temperature case, the CO quench level can lie in the CO-dominated region, and CO remains the primary carbon source. However, the T-P profile prefers CH_4 over CO in the infrared photosphere. Thus, the high internal temperature of the exoplanets' T-P profile can quench CO in the CO-dominated region, and methane can be depleted in the infrared photosphere. There is a discrepancy between the distribution of the observed radii of the hot Jupiters and the planetary evolution model, which is known as the radius anomaly (Thorngren and Fortney 2018). A possible explanation of

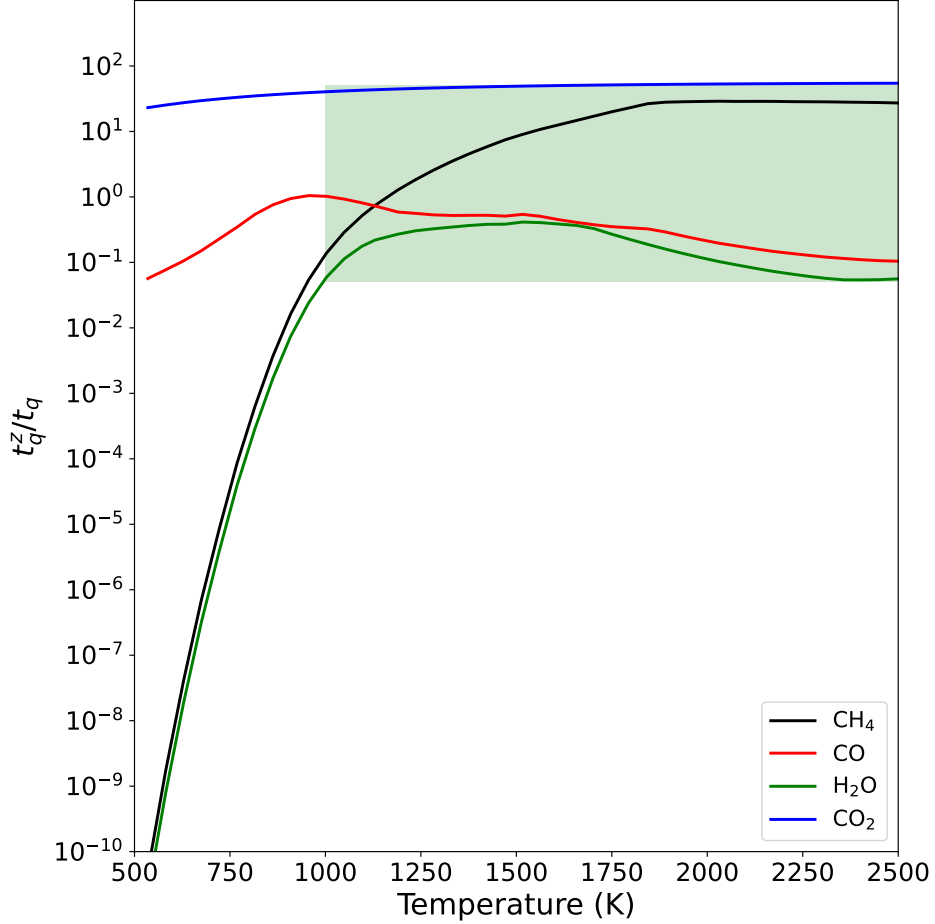


Figure 25. The ratio of the chemical timescale obtained in our study (t_q) and from Zahnle and Marley (2014) (t_q^z) are shown, for the thermal profile shown in Figure 24.

the radius anomaly is the high internal temperature (Fortney et al. 2021). Thus high internal temperature and high metallicity can result in CH_4 depletion.

6.2. Effect of Clouds and Hazes

The change in the thermal structure can alter the position of the quench level. In the present study, the thermal profile is taken as an input parameter. The clouds of $\text{H}_2\text{O}-\text{CH}_4$ are formed at 100-400 K for 10^2 to 10^{-3} bar, which does not fall in the parameter space that we studied. However, the presence of other clouds (e.g., MgSiO_3 , Mg_2SiO_4 , Al_2O_3 , Na_2S , KCl) formed in the parameter range can affect the thermal structure of the atmosphere (Marley et al. 2013; Madhusudhan et al. 2016; Poser et al. 2019). The production of hazes from the photodissociation of $\text{CH}_4-\text{HCN}-\text{C}_2\text{H}_2$ also affects the atmospheric extinction and contributes to shaping the thermal profile of the atmosphere (Kawashima and Ikoma 2019). In this study we have used the solar C/O ratio which is adopted from Lodders et al. (2009), thus our results are not valid for any atmosphere with a different C/O ratio. The mineral clouds (like silicates) can remove a significant amount of O (Madhusudhan et al. 2016), and the resulting C/O ratio can deviate from the value we have used in this study. Investigating the effect of clouds and hazes on the quench level is beyond the scope of this study. We focus on the

general effect of metallicity on the quench level rather than on particular exoplanets, which makes this study independent of the presence of clouds and hazes.

6.3. *Effect of C/O vs Metallicity*

In our study, we fixed the C/O ratio to the solar value. However, for a different C/O ratio, the result in this study can change. The change in the C/O ratio changes the bulk abundance of C with respect to O. This results in changes in the equilibrium composition of the atmosphere, leading to a change in the chemical timescale of the species (Madhusudhan 2012; Moses et al. 2013b,a). Tsai et al. (2018) explored the effect of C/O ratio on the conversion pathways of $\text{CO} \rightleftharpoons \text{CH}_4$. They found that for $\text{C/O} > 1$, C_2H_4 , C_2H_3 , and C_2H_2 also come as intermediate molecules in the conversion of $\text{CO} \rightleftharpoons \text{CH}_4$. For solar C/O ratio, H_2O and CO_2 remain in equilibrium, and quenching does not affect the H_2O abundance, as H_2O is the major O species at the quench level. Moreover, the $\text{CO}_2 \rightleftharpoons \text{CO}$ conversion is relatively fast, and CO_2 remains in equilibrium with H_2O and CO . However, for the super-solar C/O ratio, H_2O and CO_2 can quench deep in the atmosphere resulting in a more pronounced effect of transport on these molecules. In our future work, we will analyze the effect of the C/O ratio in the parameter space.

7. CONCLUSION

We present a detailed study of the effect of atmospheric metallicity on the abundance of $\text{CO}-\text{CH}_4-\text{CO}_2-\text{H}_2\text{O}$ in the presence of transport. We have used the quenching approximation to find the effect on the quenched abundance. We have made a 3D grid in the temperature (500 to 2500 K), pressure (0.01 mbar to 1 kbar), and metallicity ($0.1-1000 \times$ solar metallicity) space for this study. We first calculate the chemical equilibrium abundance at the grid points and use a network analysis tool to find the RLS in the conversion of $\text{CH}_4 \rightleftharpoons \text{CO}$. We then use the RLS to find the chemical timescale and compare it with the vertical mixing timescale of the atmosphere to find the quench levels. We find all possible quench levels in the grid and then use the quench level data to understand the effect of metallicity on the abundance of $\text{CO}-\text{CH}_4-\text{CO}_2-\text{H}_2\text{O}$. Our conclusions are as follows:

- The equilibrium abundance profiles are in accordance with Moses et al. (2013b); Zahnle and Marley (2014); Venot et al. (2014). The CO, H_2O , and CO_2 abundances increase with metallicity; however, the CH_4 abundance increases only in the CH_4 dominant region. The equal-abundance curve of CH_4 and CO divides the temperature-pressure space of $\text{CH}_4-\text{CO}-\text{CO}_2-\text{H}_2\text{O}$ into two regions. In the CO dominant region, CH_4 , CO and CO_2 vary as $\approx [\text{Fe}/\text{H}]^0$, $\approx [\text{Fe}/\text{H}]^1$, $\approx [\text{Fe}/\text{H}]^2$ respectively. However, in the CH_4 dominant region, the increment in CH_4 is proportional to the metallicity, while CO and CO_2 increase more rapidly with metallicity than in the first region.
- The metallicity changes the dominance area of RLS in temperature-pressure space. In the area where atomic hydrogen is dominant over H_2 (above the 10^{-8} bar-1750 K to 10^{-3} bar-2500 K, see Figure 4), the different dehydrogenation ($\text{CH}_4 \rightarrow \text{CO}$) or hydrogenation ($\text{CO} \rightarrow \text{CH}_4$) reactions become RLS. For most of the temperature-pressure range, the RLS of $\tau_{\text{H}_2\text{O}}$ is the same as the RLS for τ_{CH_4} . However, for high-temperature and low-pressure region, the C atom for the conversion of H_2O into CO comes from HCN and CN. The RLS of this region does not follow the RLS of τ_{CH_4} .

- In the conversion of $\text{CH}_4 \rightarrow \text{CO}$, the $\text{H}_2 \rightleftharpoons \text{H}$ conversion also plays an important part. The $\text{H}_2 \rightleftharpoons \text{H}$ conversion term increases with metallicity as this term is proportional to the CO abundance. However, the timescale of the rate-limiting step decreases with metallicity which makes τ_{CH_4} a complex function of metallicity. In converting $\text{CO} \rightarrow \text{CH}_4$, the $\text{H}_2 \rightleftharpoons \text{H}$ conversion term contributes only for $[\text{Fe}/\text{H}] = 3$, $T < 1000$ K, $P > 10^2$ bar, and for other parameter ranges the RLS term mostly contribute to τ_{CO} . The timescale of the RLS decreases with metallicity for $P < 10^{-3}$ bar and $T \gtrsim 2250$ K, and for other parameter ranges it is not affected by the metallicity.
- We compare the vertical mixing and chemical timescale to study the effect of metallicity on the quench level. For a fixed value of η ($\tau_{mix} = (\eta H)^2 / K_{zz}$), the vertical mixing timescale is decreased by two orders of magnitude as the metallicity increases from 0.1 to $1000 \times$ solar metallicity. Moreover, the CH_4 timescale changes by four orders of magnitude, and the CO timescale changes by less than one order of magnitude. So the quench level of CO follows the vertical mixing timescale, and the quench level of CH_4 follows the chemical timescale. CO quenches at a higher pressure compared to the CH_4 quench level. For high internal temperature, this favors CO over CH_4 in the transport-dominated region, as CO quenches in the atmospheric region where CO dominates over CH_4 . The CO quench level moves to the high-pressure region with an increase in metallicity. However, the quench level of CH_4 shifts towards low pressure with metallicity, where the $\text{H}_2 \rightleftharpoons \text{H}$ conversion term dominates in τ_{CH_4} .
- We have compared the quenching approximation result for two exoplanets for CO and CH_4 with the photochemistry-transport model. For GJ 1214 b, the CO abundance is accurate within \approx a factor of five for low metallicity. For high metallicity, this is accurate within \approx a factor of two. In the case of CH_4 , this is accurate within \approx a factor of two for low metallicity. For high metallicity, it is accurate within \approx a factor of seven. For HD 189733 b, the CO abundance is accurate within \approx a factor of two. However, for CH_4 , it is accurate within \approx an order of magnitude. The accuracy of the quenching approximation can improve significantly by incorporating the mixing length using the method given by [Smith \(1998\)](#). However, we do not include this method here as we only test the quenching approximation for a broad range of parameters and do not aim to constrain the abundance for a specific exoplanet.
- We use the quench level data to constrain the mixing strength and atmospheric metallicity for four exoplanets, namely HR 8799 b, HD 189733 b, GJ 436 b, and WASP-39 b. For HR 8799 b and HD 189733 b, we find that observation constrains of CH_4 and CO abundance along with the quench level data can constrain the metallicity and K_{zz} . However, for GJ 436 b, we can constrain only the metallicity using the CO abundance, whereas the observed CH_4 abundance is indicative of a higher C/O ratio in the atmosphere.

ACKNOWLEDGEMENTS

The authors thank the anonymous referee for constructive comments which strengthened the paper. We thank Nikku Madhusudhan for his helpful insights, for reading the manuscript, and giving valuable suggestions to improve this work. We thank Sana Ahmed for suggestions that improved the overall

readability of the manuscript. The work done at the Physical Research Laboratory is supported by the Department of Space, Government of India.

APPENDIX

A. PHOTOCHEMISTRY-TRANSPORT MODEL

We have developed a FORTRAN-based 1D atmospheric model that deals with the transport and photochemistry disequilibrium processes. The model uses the plane-parallel approximation and divides the atmosphere into N layers, and solves the mass continuity equation for each species in the network in each layer. The model requires the following input parameters:

- Thermal profile of the atmosphere.
- Initial mixing ratio of the atmosphere or elemental abundance.
- Eddy diffusion coefficient to mimic the turbulent mixing.
- The host star flux at the top of the atmosphere for calculating the photochemical reaction rates.
- Physical parameters of the exoplanet, such as surface gravity.
- Boundary conditions at the top and bottom of the atmosphere.
- Chemical network.

A.1. Governing Equations

To find the atmospheric composition, the 1D atmospheric model solves the coupled one-dimensional mass continuity equation:

$$\frac{\partial n_i}{\partial t} = P_i - n_i L_i - \frac{\partial \phi_i}{\partial z}, \quad (\text{A1})$$

$$P_i = \sum_{j=1, m_{ji}>0}^{N_R} K_j m_{ji} \prod_{k=1, m_{jk}>0}^{N_s} n_k^{m_{jk}},$$

$$n_i L_i = \sum_{j=1, m_{ji}<0}^{N_R} K_j m_{ji} \prod_{k=1, m_{jk}>0}^{N_s} n_k^{m_{jk}},$$

where n_i , P_i , and L_i are the number density, the production and the loss rate of the i -th chemical species. N_R , N_s , and K_j are the total number of reactions, the total number of species, and the rate constant of the j -th reaction in the network. m_{ji} is the stoichiometric coefficient of the j -th reaction of the i -th species [Laidler \(1996\)](#), and ϕ_i is the transport flux of the i -th species. This transport flux includes Eddy diffusion and molecular diffusion and has the following form adopted from [Hu et al. \(2012\)](#):

$$\phi_i = \phi_{i,E} + \phi_{i,m} = -Kn \frac{\partial f_i}{\partial z} - Dn \frac{\partial f_i}{\partial z} + Dn \left[\frac{1}{H} - \frac{1}{H_i} - \alpha_T \frac{1}{T} \frac{dT}{dz} \right]. \quad (\text{A2})$$

The Eddy and molecular diffusion fluxes for the i -th species are $\phi_{i,E}$ and $\phi_{i,m}$ respectively. K and D are the Eddy and molecular diffusion coefficients. H and H_i are the mean scale height and the molecular scale height respectively, and α_T is the thermal diffusion factor [Hu et al. (2012), Banks and Kockarts (1973)]. The transport processes are required to simulate atmospheric mixing, which is one of the physical processes responsible for changing the atmospheric composition from its chemical equilibrium abundance. The first term on the right-side in Equation A2 is the Eddy diffusion term, mimicking 3D mixing in a 1D model. The last two terms represent molecular diffusion in the atmosphere. The molecular diffusion caused an uplift in the lighter species in the atmosphere, and the heavier species tend to settle down. As a result, the species are settled at different heights and the atmosphere becomes layered (Madhusudhan et al. 2016).

In general, in the high-pressure and high-temperature regions of the atmosphere, where the chemical timescale is small compared to the mixing timescale, the atmospheric abundance follows the chemical equilibrium abundance. In the low-pressure and low-temperature regions of the atmosphere, the mixing timescale becomes smaller than the chemical timescale, and transport changes the atmospheric abundance from its chemical equilibrium abundance. Prinn and Barshay (1977) used the transport mixing for the first time and found that the high abundance of CO in the upper atmosphere of Jupiter is the result of the transport of CO from the high-pressure region where it is stable. In continuation, several studies use Eddy and molecular diffusion in 1D models to include the transport processes (Allen et al. 1981; Line et al. 2011; Hu et al. 2012; Madhusudhan 2012; Visscher 2012; Krasnopolsky 2013; Moses et al. 2013a,b; Agúndez et al. 2014; Hu et al. 2015; Rimmer and Helling 2016; Tsai et al. 2017; Rimmer et al. 2021). The gas kinetics theory can calculate the molecular diffusion coefficient, and here we adopted the method given by Chapman and Cowling (1991). The Eddy diffusion coefficient has large uncertainty and can be calculated by multiplying the mixing length with the characteristic speed of convection. The mixing length cannot be calculated from the first principle as it is a chaotic function of many atmospheric parameters. However, one can constrain it by the 3D general circulation model (Heng 2017; Madhusudhan et al. 2016).

The solution we seek for Equation A1 is a set of abundances of chemical species for which the right side of Equation A1 is zero. In another way, the total production, loss, and transport are summed up to zero for a steady-state solution (assuming the parameters are fixed for the system). The discretized version of Equations A1 and A2 are as follows:

$$\begin{aligned} \frac{\partial n_{z,i}}{\partial t} &= P_{z,i} - L_{z,i} - \frac{\phi_{z+1/2,i} - \phi_{z-1/2,i}}{\Delta Z} \\ \phi_{z+1/2} &= \phi_{z+1/2,i}^{Eddy} + \phi_{z+1/2,i}^{molecular} \\ &= -K_{z+1/2} N_{z+1/2} \frac{f_{z+1,i} - f_{z,i}}{\Delta Z} - D_{z+1/2,i} N_{z+1/2} \frac{f_{z+1,i} - f_{z,i}}{\Delta Z} \\ &\quad + D_{z+1/2,i} N_{z+1/2} \frac{f_{z+1,i} + f_{z,i}}{2} \left[\frac{m_z g}{k_b T_{z+1/2}} - \frac{m_{z,i} g}{k_b T_{z+1/2}} - \alpha_T \frac{1}{T_{z+1/2}} \frac{T_{z+1} - T_z}{\Delta Z} \right], \end{aligned}$$

and the governing equation in the discretization form is as follows:

$$\begin{aligned} \frac{\partial n_i}{\partial t} = & P_i - L_i + \left(k_{i+1/2} \frac{N_{i+1/2}}{N_{i+1}} - d_{i+1/2} \frac{N_{i+1/2}}{N_{i+1}} \right) n_{i+1} \\ & - \left(k_{i+1/2} \frac{N_{i+1/2}}{N_i} + d_{i+1/2} \frac{N_{i+1/2}}{N_i} + k_{i-1/2} \frac{N_{i-1/2}}{N_i} - d_{i-1/2} \frac{N_{i-1/2}}{N_i} \right) n_i \\ & + \left(k_{i-1/2} \frac{N_{i-1/2}}{N_{i-1}} + d_{i-1/2} \frac{N_{i-1/2}}{N_{i-1}} \right) n_{i-1}. \end{aligned}$$

i and z indices run in species and the atmospheric layers, so the number of coupled equations are $N_{layers} \times N_{species}$. k_b , m_z , and $m_{z,i}$ are the Boltzmann constant, the mean molecular mass, and i -th species mass in z -th atmospheric layer. g is the gravity of the planet at the z -th atmospheric layer, T_z is the temperature, and $f_{z,i}$ is the mixing ratio of the i -th species at the z -th layer. Here, the aim is to find a set of species in each layer, so that the right side of the equation is zero for all the species in all the layers, which also satisfies the boundary condition. To do this, we first take a set of relevant initial abundances and evolve the system with time. The reaction rates vary over 20-30 orders of magnitude, making these equations stiff. Therefore, to arrive at numerical solutions, we use the semi-implicit Rosenbrock fourth-order integration method which can handle the stiffness of these equations (Rosenbrock 1963; Shampine 1982).

A.2. Chemical Network

Our primary chemical network is taken from Rimmer and Helling (2016) and Rimmer and Rugheimer (2019), in which we keep the chemical network from Tsai et al. (2017) as a complete subset, i.e., for the reactions which are common to both the networks, we used the reaction rates from Tsai et al. (2017). Our network includes 350 chemical species which are made up of H, C, N, O, He, Na, Mg, Si, Cl, Ar, K, Ti, and Fe elements. These species are interconnected by more than 5000 chemical reactions. These reactions include two-body neutral-neutral and ion-neutral reactions, three-body neutral and dissociation reactions, thermal ionization and recombination reactions, and photochemical reactions. Rimmer and Helling (2016) and Rimmer and Rugheimer (2019) compiled the network using reactions from NIST (J. A. Manion and Frizzell 2015), KIDA (Wakelam et al. 2012), Ikezoe (1987); Sander et al. (2011); Tsai et al. (2017). Due to the availability of the VULCAN code from Tsai et al. (2017, 2021), we use it for the benchmarking of our model outputs with the VULCAN output. For this benchmarking, the network is adopted from Tsai et al. (2017, 2021), which contains 55 chemical species made up of H-C-N-O elements. These species are interconnected by 640 chemical reactions. In the network, 250 are two-body reactions, 50 are three-body reactions, and 40 are photochemical reactions. The two-body and three-body reactions are reversible in the network, and the network is benchmarked for a temperature range of 500 to 2500 K in Tsai et al. (2017). The 55 species are H, H₂O, OH, H₂, O, CH, C, CH₂, CH₃, CH₄, C₂, C₂H₂, C₂H, C₂H₃, C₂H₄, C₂H₅, C₂H₆, CO, CO₂, CH₂OH, H₂CO, HCO, CH₃O, CH₃OH, CH₃CO, O₂, H₂CCO, HCCO, N, NH, CN, HCN, NO, NH₂, N₂, NH₃, N₂H₂, N₂H, N₂H₃, N₂H₄, HNO, H₂CN, HNCO, NO₂, N₂O, C₄H₂, CH₃NH, CH₂NH, CH₂NH₂, CH₃NH₂, CH₃CHO, HNO₂, O(¹D), CH₂(¹D), He.

The rate constants of the two-body neutral-neutral, ion-neutral, and dissociative recombination reactions are calculated by the generalized Arrhenius equation (Heng and Lyons 2016)

$$k = \alpha \left(\frac{T}{300 \text{ K}} \right)^\beta \exp \left(-\frac{\gamma}{T} \right), \quad (\text{A3})$$

where k ($\text{cm}^3 \text{s}^{-1}$) is the rate coefficient of the reaction, and α , β , and γ are the Arrhenius coefficients for the specific reaction.

In a three-body reaction, the two reactants will combine to form one product in the presence of a third body. The three-body reactions in the network include neutral reactions, dissociation reactions, and thermal ionization and recombination reactions. The rate constant of three body reaction is calculated using low and high-pressure rates, which are computed using the modified Arrhenius expression:

$$k_o = \alpha_o \left(\frac{T}{300 \text{ K}} \right)^{\beta_o} \exp \left(-\frac{\gamma_o}{T} \right), \quad (\text{A4})$$

$$k_\infty = \alpha_\infty \left(\frac{T}{300 \text{ K}} \right)^{\beta_\infty} \exp \left(-\frac{\gamma_\infty}{T} \right), \quad (\text{A5})$$

where k_o ($\text{cm}^6 \text{s}^{-1}$) and k_∞ ($\text{cm}^3 \text{s}^{-1}$) are the low-pressure and high-pressure rate constants. The rate constant of a three body reaction in terms of low and high-pressure rate constants is as follows:

$$k = \frac{k_o[M]}{1 + \frac{k_o}{k_\infty}[M]}, \quad (\text{A6})$$

where $[M]$ is the number density of the neutral third species. We refer the reader to see §2 in [Rimmer and Helling \(2016\)](#) and §4 in [Tsai et al. \(2017\)](#) for a detailed discussion on calculating different rate constants of reactions used in this model.

A.2.1. Photochemical Rate Constants

The rate constant of photodissociation reactions is a function of the number density of photons, the branching ratio of the dissociation path (quantum yield), and the wavelength-dependent cross-section. The required photon density for the photodissociation rate constant is calculated using the two-stream approximation of radiative transfer. The rate for photodissociation reaction is calculated as follows:

$$k = \int_{\lambda} \sigma(\lambda) N_{\lambda} \times BR \times d\lambda \quad (\text{A7})$$

where $\sigma(\lambda)$ is the cross-section of the species, N_{λ} is the number of photons in $[\lambda, \lambda + d\lambda]$ and BR is the branching ratio ([Hu et al. 2012](#)).

If the radiation passes through some medium, it gets scattered, absorbed, or re-emitted in the medium itself. In the exoplanet atmosphere, the stellar radiation also gets scattered or absorbed in the atmosphere (for the time being, we ignore the re-emitted photon) that distributes the photon density in each atmospheric layer. The photochemistry will only depend upon the total number of photons present in the atmospheric layers. In order to find the photon flux in each layer, we have used the two-stream approximation to find the available photon count in each atmospheric layer. The two-stream approximation is a well known radiative transfer formulation which can efficiently compute the radiation propagation in the atmosphere ([Toon et al. 1989](#); [Hu et al. 2012](#); [Heng et al. 2014](#); [Heng 2017](#); [Malik et al. 2017](#)). It only considers the vertical propagation of radiation. The horizontal

propagation is negligible as we assume that the thickness of the atmosphere is incomparable to the radius of the planet. Depending upon the physical processes and parameter space, the equation for the two-stream approximation can take different forms, and here, we have used the two-stream approximation in the limit of coherent and isotropic scattering (Heng et al. 2014).

$$\begin{aligned}
F_{\uparrow j} &= A_1 \zeta_+ e^{\alpha \tau'_j} + A_2 \zeta_- e^{-\alpha \tau'_j} + \pi B_{j+}, \\
F_{\downarrow j} &= A_1 \zeta_- e^{\alpha \tau'_j} + A_2 \zeta_+ e^{-\alpha \tau'_j} + \pi B_{j-}, \\
B' &= \frac{\partial B}{\partial \tau} = \frac{B_j - B_{j-1}}{\tau_j - \tau_{j-1}}, \\
B_{j-} &= B_1 + B'(\tau_j - \tau_{j-1}) - \frac{B'}{2}, \\
B_{j+} &= B_2 + B'(\tau_{j-1} - \tau_j) + \frac{B'}{2}, \\
\zeta_{\pm} &= \frac{1}{2}[1 \pm (1 - \omega_0)^{\frac{1}{2}}].
\end{aligned} \tag{A8}$$

The index j represents the j -th atmospheric layer, and $F_{\uparrow j}$ and $F_{\downarrow j}$ are the outgoing and incoming flux in this layer. A_1 and A_2 are the integration constants which are calculated by the boundary condition. θ , τ , ω_0 and B are the polar angle in spherical coordinates, optical depth, single-scattering albedo and Planck function respectively. $\mu = \cos(\theta)$ and $\tau' = \frac{\tau}{\mu}$ is the slant optical depth. We refer the reader to see the full derivation of Equation A8 in Heng et al. (2014).

Using the boundary condition, Equation A8 becomes

$$\begin{aligned}
F_{\uparrow 1} &= \frac{1}{(\zeta_- \mathbf{T})^2 - \zeta_+^2} \left[(\zeta_-^2 - \zeta_+^2) \mathbf{T} F_{\uparrow 2} - \zeta_- \zeta_+ (1 - \mathbf{T}^2) F_{\downarrow 1} \right. \\
&\quad \left. + \pi B_{1+} (\zeta_-^2 \mathbf{T}^2 - \zeta_+^2) + B_{2+} \mathbf{T}^2 (\zeta_+^2 - \zeta_-^2) + B_{1-} \zeta_+ \zeta_- (1 - \mathbf{T}^2) \right], \\
F_{\downarrow 2} &= \frac{1}{(\zeta_- \mathbf{T})^2 - \zeta_+^2} \left[(\zeta_-^2 - \zeta_+^2) \mathbf{T} F_{\downarrow 1} - \zeta_- \zeta_+ (1 - \mathbf{T}^2) F_{\uparrow 2} \right. \\
&\quad \left. + \pi B_{2-} (\zeta_-^2 \mathbf{T}^2 - \zeta_+^2) + B_{1-} \mathbf{T}^2 (\zeta_+^2 - \zeta_-^2) + B_{2+} \zeta_+ \zeta_- (1 - \mathbf{T}^2) \right],
\end{aligned} \tag{A9}$$

where $\mathbf{T} = e^{-D\delta\tau}$ and $\delta\tau = \tau_2 - \tau_1$. Equation A9 is the two-stream solution for the radiation transfer between two consecutive boundary layers. The solution to this equation will give the diffuse radiation flux.

A.2.2. Reverse Reaction Rate Constant

To calculate the reverse reaction rate constant, we use the method described in Burcat et al.; Heng and Lyons (2016); Tsai et al. (2017). The forward reaction whose rate constant is k_f has the following form:



The reverse reaction of the above forward reaction with reverse rate constant (k_r) is the following:



In chemical equilibrium, the forward and reverse reaction rates will become equal, and the ratio of the forward rate constant and the reverse rate constant is called the equilibrium constant (k_c) of the reaction or $k_c = k_f/k_r$. This equilibrium constant can be calculated using the thermodynamic coefficient (thermodynamic coefficient is the fitted coefficient of the polynomial fit of enthalpy and entropy in temperature space). The equation for the same is given below.

$$k_c = (RT)^{\Delta\nu} \exp \left(\Delta a_1 (\log T - 1) + \Delta a_2 T/2 + \Delta a_3 T^2/6 + \Delta a_4 T^3/12 + \Delta a_5 T^4/20 - \Delta a_6/T + \Delta a_7 \right),$$

where R is the gas constant, $\Delta\nu$ is the difference between the number of reactants and the number of products, T is the temperature in K and $\Delta a_i = a_i(C + D + E) - a_i(A + B)$, $i \in [1, 7]$. a_i are the thermodynamic coefficients for the species that take part in the reaction. The reverse rate constant is given by the ratio of the forward rate constant and the equilibrium constant ($k_r = k_f/k_c$). The thermodynamic coefficients data is taken from NASA-CAE database and [Burcat et al.](#).

A.3. Benchmarking

In this section, we benchmark our disequilibrium model (transport and photochemistry) with the VULCAN model ([Tsai et al. 2017, 2021](#)). For the benchmarking, we have calculated the chemical composition of HD 189733 b from our Fortran-based 1D model and from the open source VULCAN model. We have used the day averaged thermal profile ([Moses et al. 2011; Tsai et al. 2017](#)), and constant Eddy diffusion coefficient $K_{zz} = 10^9 \text{ cm}^2 \text{ s}^{-1}$. We turn off condensation in VULCAN, as

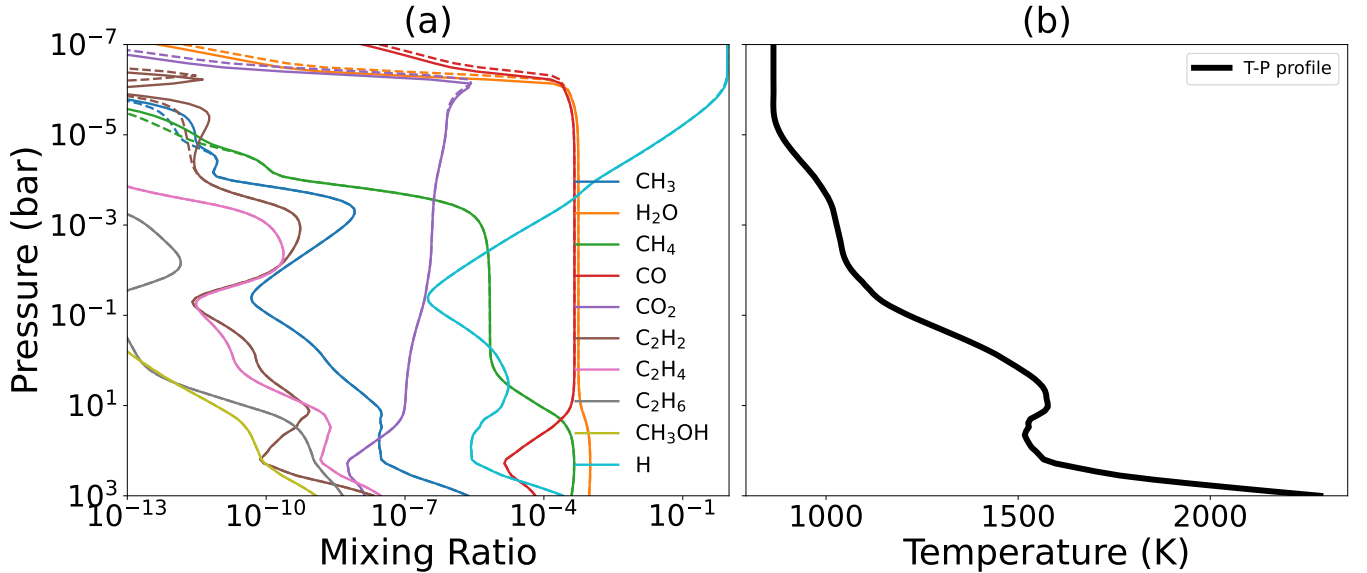


Figure 26. (a) The disequilibrium mixing ratio of HD 189733 b. The mixing ratios shown in dashed lines are calculated from our Fortran-based model and the solid lines represent the mixing ratios calculated from the VULCAN model ([Tsai et al. 2017, 2021](#)). (b) The day averaged thermal profile of HD 189733 b ([Moses et al. 2011; Tsai et al. 2017](#)).

our model does not have condensation. Figure 26 (a) shows that our results are in good agreement with the VULCAN model output, and Figure 26 (b) shows the day-averaged thermal profile of HD 189733 b. Our model output matches well with the VULCAN output in the chemical equilibrium and transport-dominated region. It is to be noted that we use a slightly different version of the integration scheme, which is probably the cause for the slight differences in the photochemistry dominated region.

REFERENCES

- Agúndez, M., Venot, O., Selsis, F., and Iro, N.: 2014, *Astrophysical Journal* **781**(2)
- Ahrer, E.-M., Stevenson, K. B., Mansfield, M., Moran, S. E., Brande, J., Morello, G., Murray, C. A., Nikolov, N. K., Petit dit de la Roche, D. J. M., Schlawin, E., Wheatley, P. J., Zieba, S., Batalha, N. E., Damiano, M., Goyal, J. M., Lendl, M., Lothringer, J. D., Mukherjee, S., Ohno, K., Batalha, N. M., Battley, M. P., Bean, J. L., Beatty, T. G., Benneke, B., Berta-Thompson, Z. K., Carter, A. L., Cubillos, P. E., Daylan, T., Espinoza, N., Gao, P., Gibson, N. P., Gill, S., Harrington, J., Hu, R., Kreidberg, L., Lewis, N. K., Line, M. R., López-Morales, M., Parmentier, V., Powell, D. K., Sing, D. K., Tsai, S.-M., Wakeford, H. R., Welbanks, L., Alam, M. K., Alderson, L., Allen, N. H., Anderson, D. R., Barstow, J. K., Bayliss, D., Bell, T. J., Blecic, J., Bryant, E. M., Burleigh, M. R., Carone, L., Casewell, S. L., Changeat, Q., Chubb, K. L., Crossfield, I. J. M., Crouzet, N., Decin, L., Désert, J.-M., Feinstein, A. D., Flagg, L., Fortney, J. J., Gizis, J. E., Heng, K., Iro, N., Kempton, E. M. R., Kendrew, S., Kirk, J., Knutson, H. A., Komacek, T. D., Lagage, P.-O., Leconte, J., Lustig-Yaeger, J., MacDonald, R. J., Mancini, L., May, E. M., Mayne, N. J., Miguel, Y., Mikal-Evans, T., Molaverdikhani, K., Palle, E., Piaulet, C., Rackham, B. V., Redfield, S., Rogers, L. K., Roy, P.-A., Rustamkulov, Z., Shkolnik, E. L., Sotzen, K. S., Taylor, J., Tremblin, P., Tucker, G. S., Turner, J. D., de Val-Borro, M., Venot, O., and Zhang, X.: 2022, *arXiv e-prints* p. arXiv:2211.10489
- Allen, M., Yung, Y. L., and Waters, J. W.: 1981, *J. Geophys. Res.* **86**, 3617
- Atreya, S. K., Crida, A., Guillot, T., Lunine, J. I., Madhusudhan, N., and Mousis, O.: 2018, *The Origin and Evolution of Saturn, with Exoplanet Perspective*, pp 5–43, Cambridge University Press
- Bailey, J., Butler, R. P., Tinney, C. G., Jones, H. R., O’Toole, S., Carter, B. D., and Marcy, G. W.: 2004, *Astrophysical Journal* **690**(1), 743
- Banks, P. M. and Kockarts, G.: 1973, *Aeronomy*
- Barman, T. S., Konopacky, Q. M., Macintosh, B., and Marois, C.: 2015, *Astrophysical Journal* **804**(1), 1
- Benneke, B.: 2015, pp 1–19
- Burcat, A., Ruscic, B., Chemistry, and of Tech., T. I. I.
- Chapman, S. and Cowling, T. G.: 1991, *The Mathematical Theory of Non-uniform Gases*
- Charbonneau, D., Berta, Z. K., Irwin, J., Burke, C. J., Nutzman, P., Buchhave, L. A., Lovis, C., Bonfils, X., Latham, D. W., Udry, S., Murray-Clay, R. A., Holman, M. J., Falco, E. E., Winn, J. N., Queloz, D., Pepe, F., Mayor, M., Delfosse, X., and Forveille, T.: 2009, *Nature* **462**(7275), 891
- Charnay, B., Meadows, V., and Leconte, J.: 2015, *Astrophysical Journal* **813**(1), 15
- Cooper, C. S. and Showman, A. P.: 2006, *The Astrophysical Journal* **649**(2), 1048
- Dash, S., Majumdar, L., Willacy, K., Tsai, S.-M., Turner, N., Rimmer, P. B., Gudipati, M. S., Lyra, W., and Bhardwaj, A.: 2022, *ApJ* **932**(1), 20
- Drummond, B., Mayne, N. J., Baraffe, I., Tremblin, P., Manners, J., Amundsen, D. S., Goyal, J., and Acreman, D.: 2018, *Astronomy and Astrophysics* **612**, 1
- Fortney, J. J.: 2018, *Modeling Exoplanetary Atmospheres: An Overview*, pp 51–88, Springer International Publishing, Cham
- Fortney, J. J., Dawson, R. I., and Komacek, T. D.: 2021, *Journal of Geophysical Research: Planets* **126**(3)
- Fortney, J. J., Visscher, C., Marley, M. S., Hood, C. E., Line, M. R., Thorngren, D. P., Freedman, R. S., and Lupu, R.: 2020, *The Astronomical Journal* **160**(6), 288
- Guillot, T.: 1999, *Planetary and Space Science* **47**(10-11), 1183
- Haynes, K., Mandell, A. M., Madhusudhan, N., Deming, D., and Knutson, H.: 2015, *Astrophysical Journal* **806**(2), 146
- Helling, C.: 2019, *Annual Review of Earth and Planetary Sciences* **47**(1), 583
- Heng, K.: 2017, *Exoplanetary Atmospheres: Theoretical Concepts and Foundations*
- Heng, K. and Lyons, J. R.: 2016, *The Astrophysical Journal* **817**(2), 149

- Heng, K., Mendonça, J. M., and Lee, J. M.: 2014, *Astrophysical Journal, Supplement Series* 215(1)
- Hu, R. and Seager, S.: 2014, *Astrophysical Journal* 784(1)
- Hu, R., Seager, S., and Bains, W.: 2012, *Astrophysical Journal* 761(2)
- Hu, R., Seager, S., and Yung, Y. L.: 2015, *Astrophysical Journal* 807(1), 8
- Ikezoe, Y., M. S. . T. M.: 1987
- J. A. Manion, R. E. Huie, R. D. L. D. R. B. J. V. L. O. W. T. W. S. M. J. W. H. V. D. K. D. B. A. E. C. A. M. T. C.-Y. L. T. C. A. W. G. M. F. W. J. T. H. R. F. H. and Frizzell, D. H.: 2015
- Kawashima, Y. and Ikoma, M.: 2019, *The Astrophysical Journal* 877(2), 109
- Knutson, H. A., Benneke, B., Deming, D., and Homeier, D.: 2014, *Nature* 505(7481), 66
- Krasnopolsky, V. A.: 2013, *Icarus* 225(1), 570
- Kreidberg, L., Bean, J. L., Désert, J. M., Line, M. R., Fortney, J. J., Madhusudhan, N., Stevenson, K. B., Showman, A. P., Charbonneau, D., McCullough, P. R., Seager, S., Burrows, A., Henry, G. W., Williamson, M., Kataria, T., and Homeier, D.: 2014, *Astrophysical Journal Letters* 793(2), 2
- Kreidberg, L., Line, M. R., Parmentier, V., Stevenson, K. B., Louden, T., Bonnefoy, M., Faherty, J. K., Henry, G. W., Williamson, M. H., Stassun, K., Beatty, T. G., Bean, J. L., Fortney, J. J., Showman, A. P., Désert, J.-M., and Arcangeli, J.: 2018, *AJ* 156(1), 17
- Laidler, K. J.: 1996, *Pure and Applied Chemistry* 68(1), 149
- Line, M. R., Knutson, H., Wolf, A. S., and Yung, Y. L.: 2014, *Astrophysical Journal* 783(2)
- Line, M. R., Liang, M. C., and Yung, Y. L.: 2010, *Astrophysical Journal* 717(1), 496
- Line, M. R., Vasisht, G., Chen, P., Angerhausen, D., and Yung, Y. L.: 2011, *Astrophysical Journal* 738(1)
- Line, M. R., Zhang, X., Vasisht, G., Natraj, V., Chen, P., and Yung, Y. L.: 2012, *Astrophysical Journal* 749(1)
- Lodders, K., Palme, H., and Gail, H. P.: 2009, *Landolt Börstein* 4B, 712
- Madhusudhan, N.: 2012, *Astrophysical Journal* 758(1)
- Madhusudhan, N.: 2019, *Annual Review of Astronomy and Astrophysics* 57, 617
- Madhusudhan, N., Agúndez, M., Moses, J. I., and Hu, Y.: 2016, *Space Science Reviews* 205(1-4), 285
- Madhusudhan, N. and Seager, S.: 2009, *Astrophysical Journal* 707(1), 24
- Madhusudhan, N. and Seager, S.: 2011, *Astrophysical Journal* 729(1)
- Malik, M., Grosheintz, L., Mendonça, J. M., Grimm, S. L., Lavie, B., Kitzmann, D., Tsai, S.-M., Burrows, A., Kreidberg, L., Bedell, M., Bean, J. L., Stevenson, K. B., and Heng, K.: 2017, *The Astronomical Journal* 153(2), 56
- Mansfield, M., Bean, J. L., Line, M. R., Parmentier, V., Kreidberg, L., Désert, J.-M., Fortney, J. J., Stevenson, K. B., Arcangeli, J., and Dragomir, D.: 2018, *AJ* 156(1), 10
- Marley, M. S., Ackerman, A. S., Cuzzi, J. N., and Kitzmann, D.: 2013, *Comparative Climatology of Terrestrial Planets* pp 1–51
- Marois, C., Macintosh, B., Barman, T., Zuckerman, B., Song, I., Patience, J., Lafrenière, D., and Doyon, R.: 2008, *Science* 322(5906), 1348
- Mikal-Evans, T., Sing, D. K., Goyal, J. M., Drummond, B., Carter, A. L., Henry, G. W., Wakeford, H. R., Lewis, N. K., Marley, M. S., Tremblin, P., Nikolov, N., Kataria, T., Deming, D., and Ballester, G. E.: 2019, *MNRAS* 488(2), 2222
- Molaverdikhani, K., Henning, T., and Mollière, P.: 2019, *The Astrophysical Journal* 883(2), 194
- Molaverdikhani, K., Henning, T., and Mollière, P.: 2020, *The Astrophysical Journal* 899(1), 53
- Moses, J. I., Line, M. R., Visscher, C., Richardson, M. R., Nettelmann, N., Fortney, J. J., Barman, T. S., Stevenson, K. B., and Madhusudhan, N.: 2013a, *Astrophysical Journal* 777(1)
- Moses, J. I., Madhusudhan, N., Visscher, C., and Freedman, R. S.: 2013b, *Astrophysical Journal* 763(1)
- Moses, J. I., Marley, M. S., Zahnle, K., Line, M. R., Fortney, J. J., Barman, T. S., Visscher, C., Lewis, N. K., and Wolff, M. J.: 2016, *The Astrophysical Journal* 829(2), 66
- Moses, J. I., Visscher, C., Fortney, J. J., Showman, A. P., Lewis, N. K., Griffith, C. A., Klippenstein, S. J., Shabram, M., Friedson, A. J., Marley, M. S., and Freedman, R. S.: 2011, *Astrophysical Journal* 737(1)

- Moutou, C., Loeillet, B., Bouchy, F., Da Silva, R., Mayor, M., Pont, F., Queloz, D., Santos, N. C., Ségransan, D., Udry, S., and Zucker, S.: 2006, *Astronomy and Astrophysics* **458(1)**, 327
- Poser, A. J., Nettelmann, N., and Redmer, R.: 2019, *Atmosphere* **10(11)**, 1
- Prinn, R. G. and Barshay, S. S.: 1977, *Science* **198(4321)**, 1031
- Rajpurohit, A. S., Allard, F., Homeier, D., Mousis, O., and Rajpurohit, S.: 2020, *Astronomy and Astrophysics* **642**, 2008
- Ranjan, S., Charbonneau, D., Désert, J. M., Madhusudhan, N., Deming, D., Wilkins, A., and Mandell, A. M.: 2014, *Astrophysical Journal* **785(2)**
- Rimmer, P. B. and Helling, C.: 2016, *The Astrophysical Journal Supplement Series* **224(1)**, 9
- Rimmer, P. B., Majumdar, L., Priyadarshi, A., Wright, S., and Yurchenko, S. N.: 2021, *ApJ* **921(2)**, L28
- Rimmer, P. B. and Rugheimer, S.: 2019, *Icarus* **329(February)**, 124
- Rosenbrock, H. H.: 1963, *The Computer Journal* **5(4)**, 329
- Rustamkulov, Z., Sing, D. K., Mukherjee, S., May, E. M., Kirk, J., and Schlawin, E.: 2022, *2(July)*
- Sander, S. P., Abbatt, J., Friedl, R. R., Barker, J. R., Burkholder, J. B., Golden, D. M., Huie, R. E., Kolb, C. E., Kurylo, M. J., Moortgat, G. K., Orkin, V. L., and Wine, P. H.: 2011, *JPL Publication 10-6, Jet Propulsion Laboratory, Pasadena* (17)
- Seager, S. and Deming, D.: 2010, *Annual Review of Astronomy and Astrophysics* **48**, 631
- Shampine, L. F.: 1982, *Implementation of Rosenbrock Methods*
- Sing, D. K.: 2018, pp 3–48
- Smith, M. D.: 1998, *Icarus* **132(1)**, 176
- Spake, J. J., Sing, D. K., Wakeford, H. R., Nikolov, N., Mikal-Evans, T., Deming, D., Barstow, J. K., Anderson, D. R., Carter, A. L., Gillon, M., Goyal, J. M., Hebrard, G., Hellier, C., Kataria, T., Lam, K. W. F., Triaud, A. H. M. J., and Wheatley, P. J.: 2021, *MNRAS* **500(3)**, 4042
- Stevenson, K. B., Line, M. R., Bean, J. L., Désert, J.-M., Fortney, J. J., Showman, A. P., Kataria, T., Kreidberg, L., and Feng, Y. K.: 2017, *The Astronomical Journal* **153(2)**, 68
- The JWST Transiting Exoplanet Community Early Release Science Team, Ahrer, E.-M., Alderson, L., Batalha, N. M., Batalha, N. E., Bean, J. L., Beatty, T. G., Bell, T. J., Benneke, B., Berta-Thompson, Z. K., Carter, A. L., Crossfield, I. J. M., Espinoza, N., Feinstein, A. D., Fortney, J. J., Gibson, N. P., Goyal, J. M., Kempton, E. M. R., Kirk, J., Kreidberg, L., López-Morales, M., Line, M. R., Lothringer, J. D., Moran, S. E., Mukherjee, S., Ohno, K., Parmentier, V., Piaulet, C., Rustamkulov, Z., Schlawin, E., Sing, D. K., Stevenson, K. B., Wakeford, H. R., Allen, N. H., Birkmann, S. M., Brande, J., Crouzet, N., Cubillos, P. E., Damiano, M., Désert, J.-M., Gao, P., Harrington, J., Hu, R., Kendrew, S., Knutson, H. A., Lagage, P.-O., Leconte, J., Lendl, M., MacDonald, R. J., May, E. M., Miguel, Y., Molaverdikhani, K., Moses, J. I., Murray, C. A., Nehring, M., Nikolov, N. K., dit de la Roche, D. J. M. P., Radica, M., Roy, P.-A., Stassun, K. G., Taylor, J., Waalkes, W. C., Wachiraphan, P., Welbanks, L., Wheatley, P. J., Aggarwal, K., Alam, M. K., Banerjee, A., Barstow, J. K., Blečić, J., Casewell, S. L., Changeat, Q., Chubb, K. L., Colón, K. D., Coulombe, L.-P., Daylan, T., de Val-Borro, M., Decin, L., Santos, L. A. D., Flagg, L., France, K., Fu, G., Muñoz, A. G., Gizis, J. E., Glidden, A., Grant, D., Heng, K., Henning, T., Hong, Y.-C., Inglis, J., Iro, N., Kataria, T., Komacek, T. D., Krick, J. E., Lee, E. K. H., Lewis, N. K., Lillo-Box, J., Lustig-Yaeger, J., Mancini, L., Mandell, A. M., Mansfield, M., Marley, M. S., Mikal-Evans, T., Morello, G., Nixon, M. C., Ceballos, K. O., Piette, A. A. A., Powell, D., Rackham, B. V., Ramos-Rosado, L., Rauscher, E., Redfield, S., Rogers, L. K., Roman, M. T., Roudier, G. M., Scarsdale, N., Shkolnik, E. L., Southworth, J., Spake, J. J., Steinrueck, M. E., Tan, X., Teske, J. K., Tremblin, P., Tsai, S.-M., Tucker, G. S., Turner, J. D., Valenti, J. A., Venot, O., Waldmann, I. P., Wallack, N. L., Zhang, X., and Zieba, S.: 2022, pp 1–3
- Thorngren, D. P. and Fortney, J. J.: 2018, *The Astronomical Journal* **155(5)**, 214
- Toon, O. B., McKay, C. P., Ackerman, T. P., and Santhanam, K.: 1989, *Journal of Geophysical Research* **94(D13)**, 287

- Tsai, S.-M., Kitzmann, D., Lyons, J. R., Mendonça, J., Grimm, S. L., and Heng, K.: 2018, *The Astrophysical Journal* **862(1)**, 31
- Tsai, S.-m., Lee, E. K. H., Powell, D., Zhang, X., Moses, J., Eric, H., Parmentier, V., Jordan, S., Hu, R., and Paris, F.: 2022
- Tsai, S.-M., Lyons, J. R., Grosheintz, L., Rimmer, P. B., Kitzmann, D., and Heng, K.: 2017, *The Astrophysical Journal Supplement Series* **228(2)**, 20
- Tsai, S.-M., Malik, M., Kitzmann, D., Lyons, J. R., Fateev, A., Lee, E., and Heng, K.: 2021, *The Astrophysical Journal* **923(2)**, 264
- Venot, O., Agúndez, M., Selsis, F., Tessenyi, M., and Iro, N.: 2014, *Astronomy and Astrophysics* **562**, 1
- Visscher, C.: 2012, *Astrophysical Journal* 757(1)
- Visscher, C. and Moses, J. I.: 2011, *Astrophysical Journal* 738(1)
- Wakeford, H. R. and Dalba, P. A.: 2020, *Philosophical Transactions of the Royal Society of London Series A* **378(2187)**, 20200054
- Wakelam, V., Herbst, E., Loison, J.-C., Smith, I. W. M., Chandrasekaran, V., Pavone, B., Adams, N. G., Bacchus-Montabonel, M.-C., Bergeat, A., Béroff, K., Bierbaum, V. M., Chabot, M., Dalgarno, A., van Dishoeck, E. F., Faure, A., Geppert, W. D., Gerlich, D., Galli, D., Hébrard, E., Hersant, F., Hickson, K. M., Honvault, P., Klippenstein, S. J., Picard, S. L., Nyman, G., Pernot, P., Schlemmer, S., Selsis, F., Sims, I. R., Talbi, D., Tennyson, J., Troe, J., Wester, R., and Wiesenfeld, L.: 2012, *The Astrophysical Journal Supplement Series* **199(1)**, 21
- Wolszczan, F.: 1992, *Nature* **359**, 710
- Zahnle, K. J. and Marley, M. S.: 2014, *Astrophysical Journal* 797(1)